Article:
Dashti Najafi, M, Kowsari, E, Reza Naderi, H et al. (2022) High-performance symmetric supercapacitor based on new functionalized graphene oxide composites with pyrimidine nucleotide and nucleoside. Journal of Molecular Liquids. 118381. ISSN: 0167-7322

https://doi.org/10.1016/j.molliq.2021.118381

High-performance symmetric supercapacitor based on new functionalized graphene oxide composites with pyrimidine nucleotide and nucleoside

Mohammad Dashti Najafi [a], Elaheh Kowsari [a, 1]*, Hamid Reza Naderi [b], Saeedeh Sarabadani Tafreshi [a], Amutha Chinnappan [c], Seeram Ramakrishna [c,] *, Nora H. de Leeuw [d,e], Ali Ehsani [f]

[a] Department of Chemistry, Amirkabir University of Technology, No. 424, Hafez Avenue, 1591634311, Tehran, Iran

[b] Novin Ebtekar Company, Exclusive Agent of Metrohm-Autolab and Dropsens Companies, Tehran, Iran

[c] Department of Mechanical Engineering, Center for Nanofibers and Nanotechnology, National University of Singapore, Singapore

[d] School of Chemistry, Cardiff University, Main Building, Park Place, Cardiff CF10 3AT, United Kingdom

[e] now at: School of Chemistry, University of Leeds, Leeds LS2 9JT, United Kingdom

[f] Department of Chemistry, Faculty of Science, University of Qom, Qom, Iran

[1] * corresponding authors

E-mail addresses: Kowsarie@aut.ac.ir (E. Kowsari) and seeram@nus.edu.sg (S. Ramakrishna)

Abstract

Delivery of cytidine triphosphate (CTP) as pyrimidine nucleotide and Cytarabine or arabinosylcytosine (Ara-C) as pyrimidine nucleoside onto the surface of graphene oxide (GO) has led to the fabrication of effective composites of functionalized graphene oxides (FGO-CTP and FGO-Ara-C). In the present study, we have compared FGO-CTP and FGO-Ara-C composites as active electrodes in a system with three electrodes for electrochemical measurement. Also, the as-prepared composites exhibited an ideal supercapacitive behavior in a symmetric capacitor. For the two electrode arrangement, a capacitance of 212 F g^{-1}, an energy density of 17.8 Wh kg^{-1} at 325 W kg^{-1}, and an outstanding life cycling was achieved for the FGO-CTP electrode within a voltage window of 0-1.3 V in 1M H_2SO_4 electrolyte, demonstrating greater electrochemical behavior compared to that of FGO-Ara-C electrode. In addition, the DFT calculations and charge density analysis resulted in more charge distribution on the GO layer of FGO-CTP than that of FGO-Ara-C, making it more effective as an electrode material for supercapacitors. Taking advantage of the facile synthesis method for introducing phosphate functional groups onto the surface of graphene oxide opens up an effective way for the fabrication of high-performance devices with large active surface area and high electrochemical ability in energy storage systems. Also, the assembled device expands the practical application areas of electrochemical energy storage devices significantly.

Keywords: Cytidine triphosphate, Cytarabine, Symmetric capacitor, Phosphate functional groups, Energy storage devices

1. Introduction

Recently, a considerable amount of research development has been dedicated to creating electrochemical supercapacitors (SCs) to incorporate highly efficient SCs with excellent performance in electrochemical energy storage due to their compact and inexpensive facilities, ease of accessibility, and environmentally friendly, and growing demands for global renewable energy systems[1–6]. Unlike batteries, supercapacitors are capable of a considerable power capacity, a great lifespan, and long cycle life but a low amount of energy density, limiting their broad applications. This suggests vital research needs to establish practical approaches to overcome serious shortcomings and increase the amount of stored energy. Consequently, with regard to the critical energy storage process of SCs, a significant number of studies have improved high-efficiency SC appliances [7–9]. Graphene has numerous important characteristics, including elevated mechanical strength, outstanding chemical stability, low weight, high surface area (2630 m^2/g), and superb electrical conductivity. The intense π-π interaction among graphene layers allows them to accumulate on the electrode, resulting in compact films[10–13]. Graphene functionalization increases the capacitance and creates anchoring sites to decorate both conductive polymers and metal oxide[14–16]. For supercapacitor applications, metal oxide (RuO_2, Fe_3O_4, TiO_2) and nanoparticles of conductive polymer coated with nanocomposites of functionalized graphene have also been studied[17–25].

Recently, Lin et al.[26] employed a solvent evaporation technique to fabricate a composite of rGO/PEDOT: PSS, which delivered 169 F g^{-1} performance, remaining 93% of its initial capacitance after 10000 continuous cycles. Wei et al.[27] achieved a capacitance of 310 F g^{-1} at 2 mV s^{-1} through applying a graphene-MnO_2 electrode material within a hybrid system. After 15000 cycles, capacitance retention as high as 95% was achieved. In another study, Thomas et al.[28] used composites of functionalized graphene aerogel (GA)[29,30] in asymmetric supercapacitors

as an effective anode material. A relatively high surface area of 328 m^2 g^{-1} along with the low electrical resistivity of GA composite resulted in specific capacitance as high as 175.8 F g^{-1} at 5 mV s^{-1}. The assembled ASCs device showed fast charge and discharge cycle, voltage window extension, and 89.6% capacitance retention next to 3000 cycles of charge and discharge. These ASC devices also represented 13.9 W h kg^{-1} energy density and 13.3 kW kg^{-1} power density.

In this research, we synthesized new functional graphene oxides blended with cytidine triphosphate (CTP) and Cytarabine (Ara-C). The morphology of fabricated composites was assessed using X-ray photoelectron spectroscopy, X-Ray Diffraction, Transmission electron microscopy, Field Emission scanning electron microscope, and Energy Dispersive X-ray Analysis methods. The electrochemical characteristics of the as-prepared samples were evaluated in a pseudocapacitance system. Cyclic voltammetry (CV), galvanostatic charge-discharge (GCD), and electrochemical impedance spectroscopy (EIS) methods in two and three-electrode configurations were measured using Electrochemical analysis. Benefitted from both electrochemical systems, the FGO-CTP composite exhibited greater energy density and specific capacitance than FGO-Ara-C due to phosphate groups (PO_4^{-3}) being present in CTP as active sites for electron transfer on the surface of graphene.

2. Experimental section

2.1. GO Sheet Preparation

Natural graphite was used to make GO nanosheets using the developed hummers' method[31]. A slurry of graphite (1.25 g), concentrated H_2SO_4 (42.3 ml), and $NaNO_3$ (1 g) were also prepared for 1 hour in an ice bath with constant stirring. Next, $KMnO_4$ (5.5 g) was gradually introduced into the mixture at 50°C for 1 hour, agitated, and cooled for 2 hours by pouring into a combination of

400 mL ice-water and 5 mL H_2O_2 (30%). The suspension was stored for two days to get a viscous brownish liquid with a high viscosity. The solid product was washed sequentially with 200 mL of HCl (30 wt. %) and 200 mL of ethanol, then filtered through a PTFE membrane with a pore size of 0.45 μm and saturated with diethyl ether. Vacuum drying was also used to dry the GO nanosheets after they were produced.

2.2. Functionalization of *FGO-CTP and FGO-Ara-C*

In this step, graphene oxide was acrylated in the presence of thionyl chloride ($SOCl_2$) for activating the group of carboxylic on its fundamental plane. Due to the reaction of GO (1.25 g) and $SOCl_2$ (25 ml) at 70 °C under reflux condition for 1 day, GO-acyl chloride (GO-Cl) was produced. The excess $SOCl_2$ was then extracted using a rotary method and washed three times using dichloromethane. Subsequently, during the reaction of GO-Cl (1.25 g) with Cytidine triphosphate (CTP) (1.25 g) in toluene at a temperature of 65 °C for 2 days under nitrogen atmosphere, the GO was functionalized with the CTP ligand as a precursor for the synthesis of FGO-CTP. The mixture was then set aside and evaporated at room temperature to achieve dark crystals. Likewise, for the synthesis of FGO-Ara-C, the same procedure and values were utilized to introduce Cytarabine (Ara-C) ligand into the GO-Cl compound[32,33]. As shown in Fig. 1, The schematic illustrates the process of all the FGO-CTP and FGO-Ara-C synthesis steps.

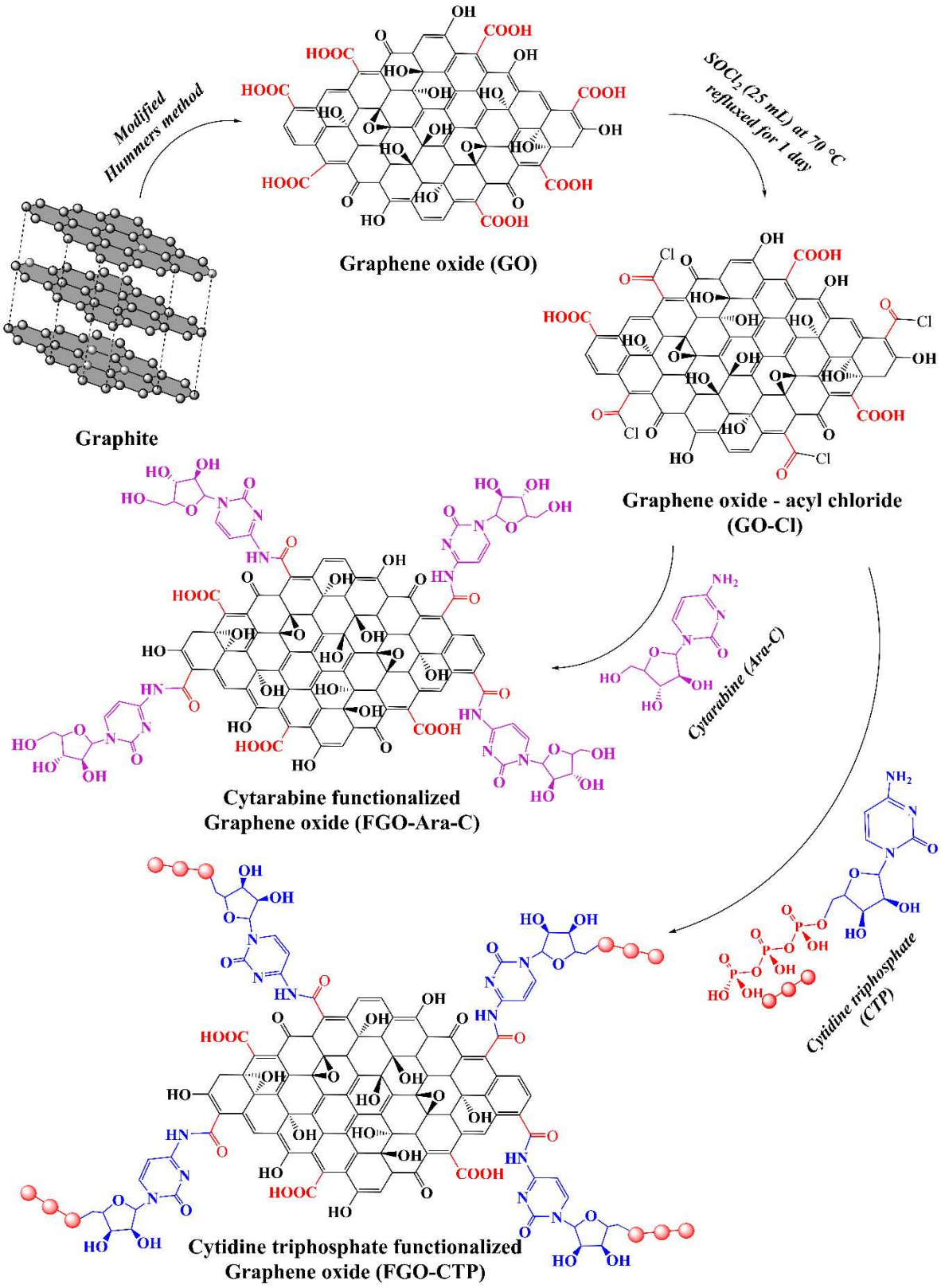

Fig. 1. Schematic procedure of all the FGO-CTP and FGO-Ara-C synthesis steps.

3. Instrumentation

3.1. Electrode Preparation

In the present study, all electrochemical procedures (CV, GCD, and EIS) were conducted by a Potentiostat/Galvanostat (Ivium V21508, Vertex) in 1M H_2SO_4 electrolyte. In order to assemble the working electrodes, a mixture of samples (FGO-CTP and FGO-Ara-C) with carbon black, graphite, and polytetrafluoroethylene (PTFE) at a mass ratio of 60:15:20:5 were blended and dispersed in ethanol. Next, the mixture was properly coated and pressed onto stainless steel (0.5 cm^2). For symmetric arrangements, each sample served as both anode and cathode electrodes on a stainless steel, with electrodes separated by a polypropylene sheet in 1M H_2SO_4 electrolyte. It is critical to remember that the mass put into symmetrical supercapacitor (SSC) devices was similar to the amount loaded into three electrode cells[7].

3.2. GO, FGO-Ara-C, and FGO-CTP characterization

X-ray photoelectron spectroscopy (XPS) was carried out using a Bes-Tec photoelectron spectrometer from Physical Electronics with Al-Kα radiation photon energy (1486.6 ± 0.2 eV). Quantera II (Physical Electronics, Minneapolis, Minnesota, USA) was chosen as the device. The Brunauer–Emmett–Teller technique was utilized for determining the pore size distribution and specific surface area with a BELSORP-mini II. FT-IR was performed on a Thermo Nicolet Avatar 360 device with KBr pellet as the background and 2 cm^{-1} spectral resolution. X-ray diffraction analysis was performed with a Cu-K diffractometer (INEL, Equinox 3000). Raman spectroscopy was performed by an Almega Thermo Nicolet Dispersive Raman spectrometer at = 514.78 nm. Images were acquired using a field-emission scanning electron microscope on a MIRA3 LM, Tuscan, at a 15.0 kV acceleration voltage. Transmission electron microscopy (model Zeiss-

EM10C Company) was used to evaluate the morphology of samples at an accelerating voltage of 100 kV.

3.3. Computational Methodology

The electron density of FGO-CTP and FGO-Ara-C was analyzed topologically in this research; prior to topological analysis, the FGO complexes were optimized using density functional theory calculations[34,35]. Calculations of hybrid DFT at the Becke Lee-Yang-Parr (B3LYP) level[36] were performed using the Vienna Ab Initio Simulation Package[37,38]. The electron-ionic core interactions were explained using Projector augmented wave potentials[39], while the Van der Waals interactions were included using Grimme's DFT-D3 method[40]. The Monkhorst-Pack[41] brillouin zone sampling method was used with the 1×1×1 k-point grid[42]. A plane-wave basis set's cutoff energy was set at 500 eV. The geometry optimization was terminated when the overall energy converged to within 10^{-5} eV and the force on each ion was less than 0.01 eV/Å.

Then, we utilized the Quantum Theory of Atoms in Molecules[43–45] to investigate the charge (electrons) distribution in two distinct materials, FGO-CTP and FGO-Ara-C. According to Bader in QTAIM, analyzing the Laplacian of the electron density distribution with atomic charges integrated over the atomic basin enables us to determine the value of the charge density concentration or depletion, the number of electrons in each compound, and their contribution to the supercapacitor's efficiency. Both structures' Laplacian of electron density was calculated and compared using the AIM-UC package[46].

4. Results and Discussion

Spectra analysis considered in the present study is accomplished applying CasaXPS software (ver.2.3) provided with the XPS method (CasaXPS, 2018). In Fig. 2a, the deconvolution XPS results in terms of GO, FGO-CTP and FGO-Ara-C are exhibited. The results for GO show the presence of oxygen (O1s 26.47 %) and carbon (C1s 73.53 %). The percentage of elements for FGO-CTP and FGO-Ara-C are indicated as C1s (81.44, 79.31%), O1s (15.77, 16.47%), and N1s (1.88, 4.21%). Accordingly, the percentage of P 2p in FGO-CTP exhibited as 0.92%, which was referred to the ligand Cytidine triphosphate (CTP). It's critical to emphasize that the presence of the principal elements of samples measured as C 1s (284.5 – 284.6 eV), O 1s (531.5 – 531.6 eV), N 1s (399.5 – 401.6 eV), and P 2p (133.6 eV). As shown in Fig. 2b and 2c, The C1s deconvolution peak for the FGO-CTP and FGO-Ara-C also indicated binding energies of C-C (284.5,284.6) C-OH (284.8, 284.9), C-N (285.9, 285.9), C=O (286.7, 286.9), C(O)N (288.05, 288.08), and C(O)O (289.06, 289.09) eV. There are three types of nitrogen bonds in the high-resolution spectrum of N 1s (Fig. S1a and S1b)[47]. Also, the N1s deconvolution peak for the FGO-CTP and FGO-Ara-C are indicated as N=C (398.02, 398.9), N-C (400.4, 400.4), and N-H (405.7, 406.1) eV. Likewise, the binding energies of O 1s for FGO-CTP indicated by the untreated substrate at 531.2, 532.3, and 533.2 eV were attributed to C/P=O, C/P-OH, and C/P-O-C, respectively (Fig. S1c)[48]. Similarly, for FGO-Ara-C binding energies of O 1s were shown as 531.1, 532.2, and 533.2 eV for C=O, C-OH, and C-O-C, respectively (Fig. S1d). The P 2p spectrum presents five types of P species (Fig. 2d), referring to P $2p_{1/2}$ (136.03 eV), P $2p_{3/2}$ (135.04 eV), P-O-C (135.2 eV), P-O (134.1 eV), and P-C (133.2 eV)[49].

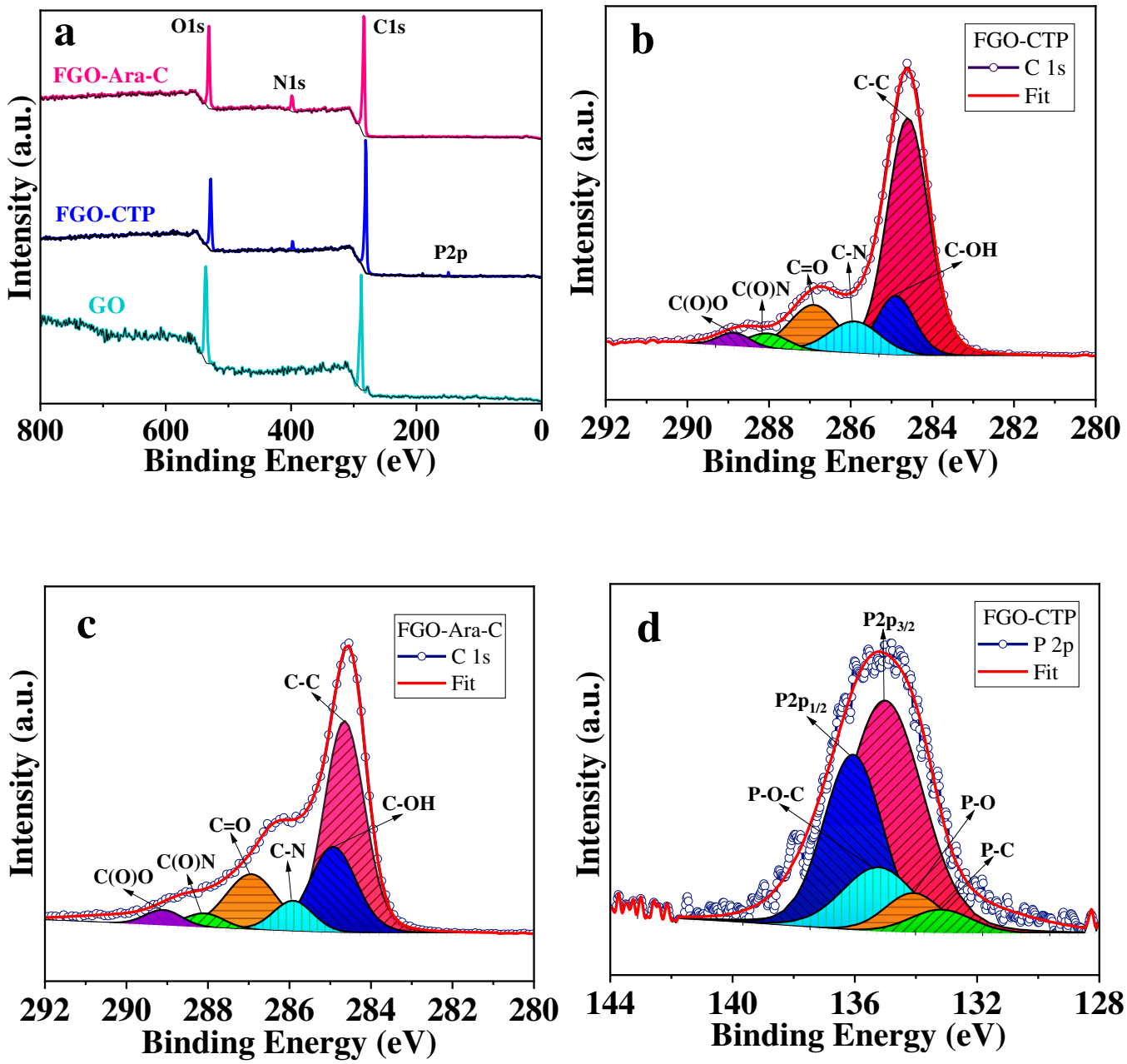

Fig. 2. (a) Deconvolution XPS results of GO, FGO-CTP, and FGO-Ara-C; Core level spectrum of C 1s as-synthesized (b) FGO-CTP and (c) FGO-Ara-C; (d) P 2p of FGO-CTP.

The surface area and pore volume of GO, FGO-CTP, and FGO-Ara-C were evaluated with nitrogen adsorption-desorption techniques. As depicted in Fig. 3a, all samples have a similar

adsorption isotherm, which due to IUPAC guidelines, could be classified as type IV. This classification is frequently applied to mesoporous and microporous materials[50]. The structural characteristics of the three samples are presented in Table. S1. The FGO-CTP and FGO-Ara-C BET surface area were found to be 45.551 and 33.759 m^2/g, while it is only 24.188 m^2/g for GO. Furthermore, three samples have comparable micropore size distributions, with the highest micropore volume recorded as 1.213 nm [51]. The observation of their distribution of pore size further confirms these findings significantly (presented in Fig. 3a). Fig. 3a depicts the pore volume of FGO-CTP and FGO-Ara-C compared to GO have been increased due to the functionalization of GO with CTP and Ara-C ligands.

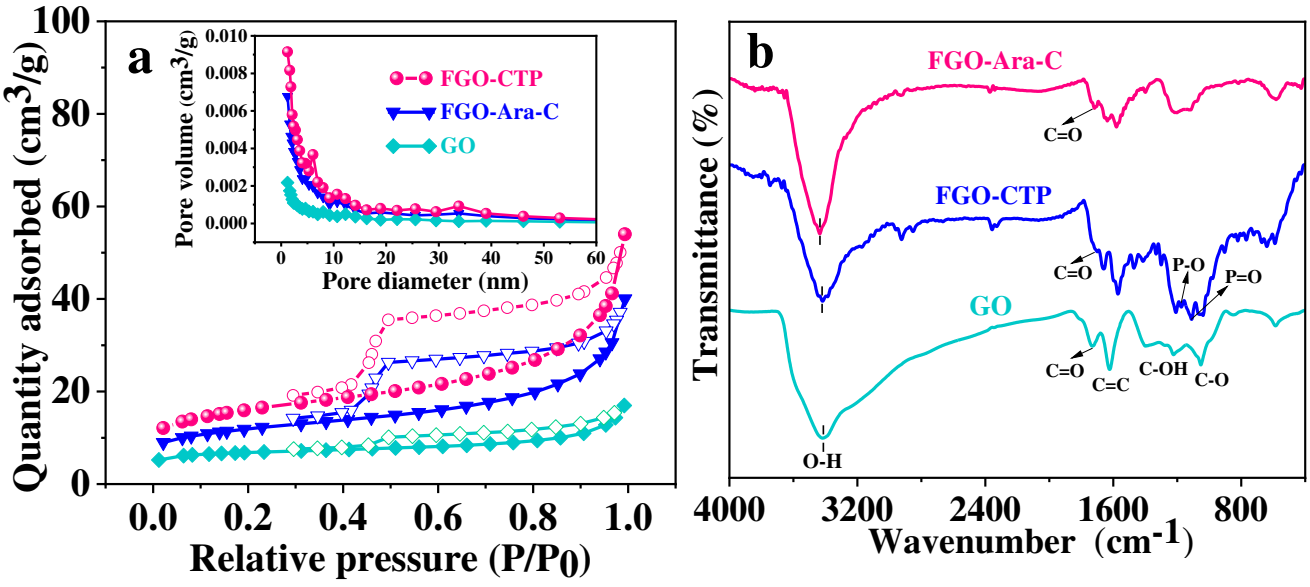

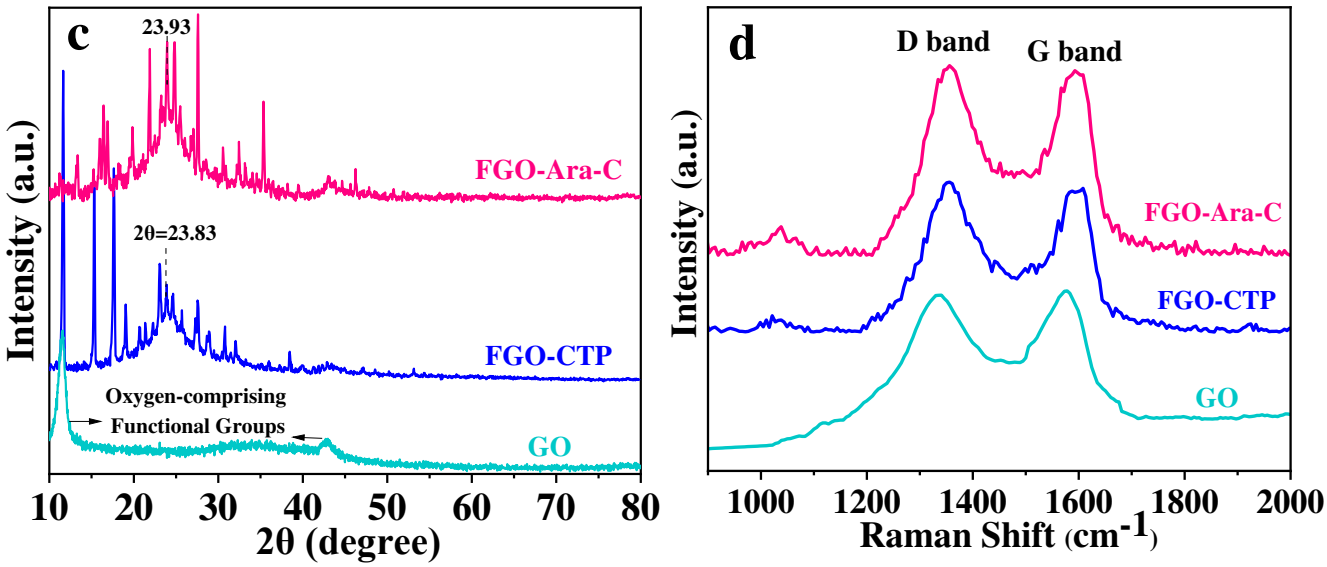

Fig. 3. (a) N_2 adsorption-desorption isotherms and pore distribution of GO, FGO-CTP, and FGO-Ara-C; (b) FT-IR spectrum of GO, FGO-CTP, and FGO-Ara-C; (c) XRD spectrum of GO, FGO-CTP, and FGO-Ara-C; (d) Raman spectra of GO, FGO-CTP, and FGO-Ara-C.

Fig. 3b compares FT-IR spectra of GO, FGO-CTP, and FGO-Ara-C. The GO spectrum exhibits strong evidence of oxygen-derived groups. For instance, different peaks including carboxylic C=O group at 1724 cm^{-1}, carboxylic C-O group at 1048 cm^{-1}, C-OH (at 1377 cm^{-1}), epoxy groups (C–O–C) at 1219 cm^{-1}, and a large broad peak about 3400 cm^{-1} were all attributable to stretching vibrations of carboxyl COOH groups establishing hydrogen bonds. Absorption bands at 1570 and 1471 cm^{-1} are assigned to the C=C expansion vibrations and C-C bonds[50]. Some similar significant peaks were found among FGO-CTP and FGO-Ara-C. The primary peaks of functional groups in FGO-CTP and FGO-Ara-C consist of N-H vibrations (3417-3434 cm^{-1}), O-H vibrations (3400 cm^{-1}), asymmetric C-H stretching vibration (2923-2928 cm^{-1}), Carbonyl stretch (1659-1718 cm^{-1}), C–N stretching vibration (1330-1399 cm^{-1}), C-O stretching vibration (1050-1054 cm^{-1})[52,53]. Fig .2b shows the vibrations peaks of P-O and P=O at 1174 and 1110 cm^{-1} besides other

typical bonds in GO, confirming the profitable functionalization route of FGO-CTP. These two peaks also confirm the presence of phosphate groups in FGO-CTP[54].

The X-ray diffraction spectra of GO, FGO-CTP and FGO-Ara-C measured within the 2θ range of from 10° to 80° are shown in Fig. 3c. They depict the graphene layers distance relating to sample oxidation. The GO exhibited a strong diffraction peak at 2θ =11° and 43°, respectively, with interlayer distances of 0.79 and 0.21 nm, respectively. The swollen basal distance is a result of intercalation of hydroxyl, carbonyl, and epoxide groups on the surface of GO. The total diffraction peak intensity of GO was reduced as a result of the chemical functionalization. In the instance of FGO-CTP and FGO-Ara-C, two maximums with similar widths have been seen at 23.83° and 23.93°, correlating to the d-spacing of 3.8 and 3.7 nm, respectively. With regards to the XRD patterns, the peaks at 2θ of 11.58°, 15.27°, 16.29°, and 27.54° for FGO-CTP and the peaks at 2θ of 13.33°, 15.98°, 16.41°, and 27.01° for FGO-Ara-C emphasize the formation of monoclinic crystal of CTP and Ara-C functional groups with successful covalent grafting on GO surface[55].

Raman analysis is shown in Fig. 3d for identifying crystal structures, both ordered and disordered, in carbonaceous materials such as graphene. For the mode of breathing induced by defect the sp^2 rings, the D peaks for GO, FGO-CTP and FGO-Ara-C appeared at 1341, 1356 and 1361 cm^{-1}, respectively[56–58]. Also, For GO, FGO-CTP and FGO-Ara-C, the peaks of G at 1573, 1592 and 1597 cm^{-1} are related to the first-order dispersion of E_2g phonon sp^2 C atoms, respectively [59]. The D band intensity is assigned to the in-plane sp^2 areas size. Moreover, the D peak intensity increase shows the creation of more sp^2 areas. The comparative intensity ratio of both peaks (I_D/I_G) calculates the disorder degree and is inversely proportional to the average size of the sp^2 clusters. The I_D/I_G ratios for FGO-CTP and FGO-Ara-C measured 1.04 and 1.02, respectively, exhibiting a

larger amount than that for GO (0.98) (Fig. 3d). The peaks observed in FGO-CTP and FGO-Ara-C at 1032 and 1038 cm^{-1} are connected to the D peak existing in the graphite whiskers[60].

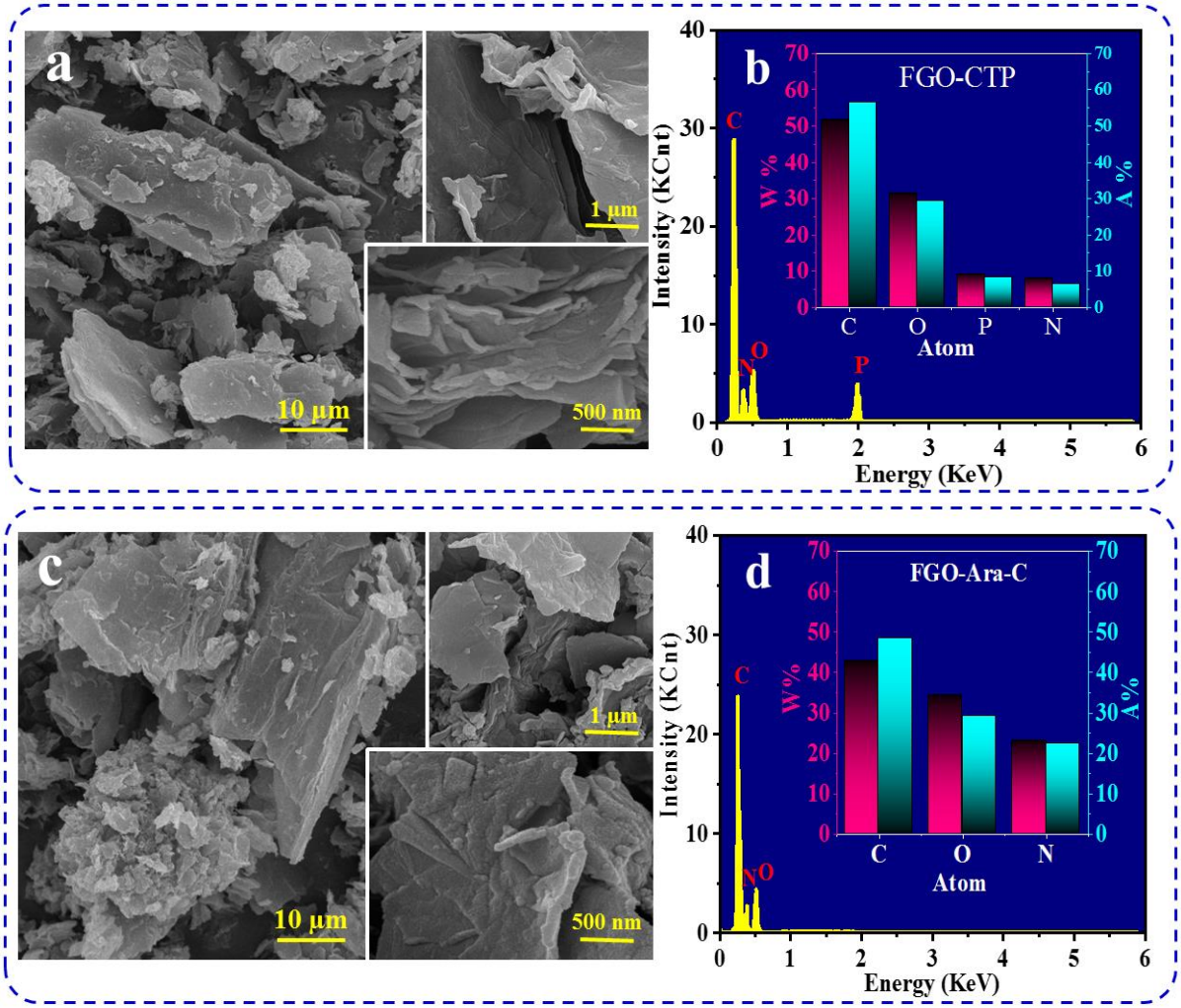

Fig. 4. FE-SEM images of synthesized a) FGO-CTP and c) FGO-Ara-C in different magnifications; EDX spectra and the percentage of presented atoms in b) FGO-CTP and d) FGO-Ara-C.

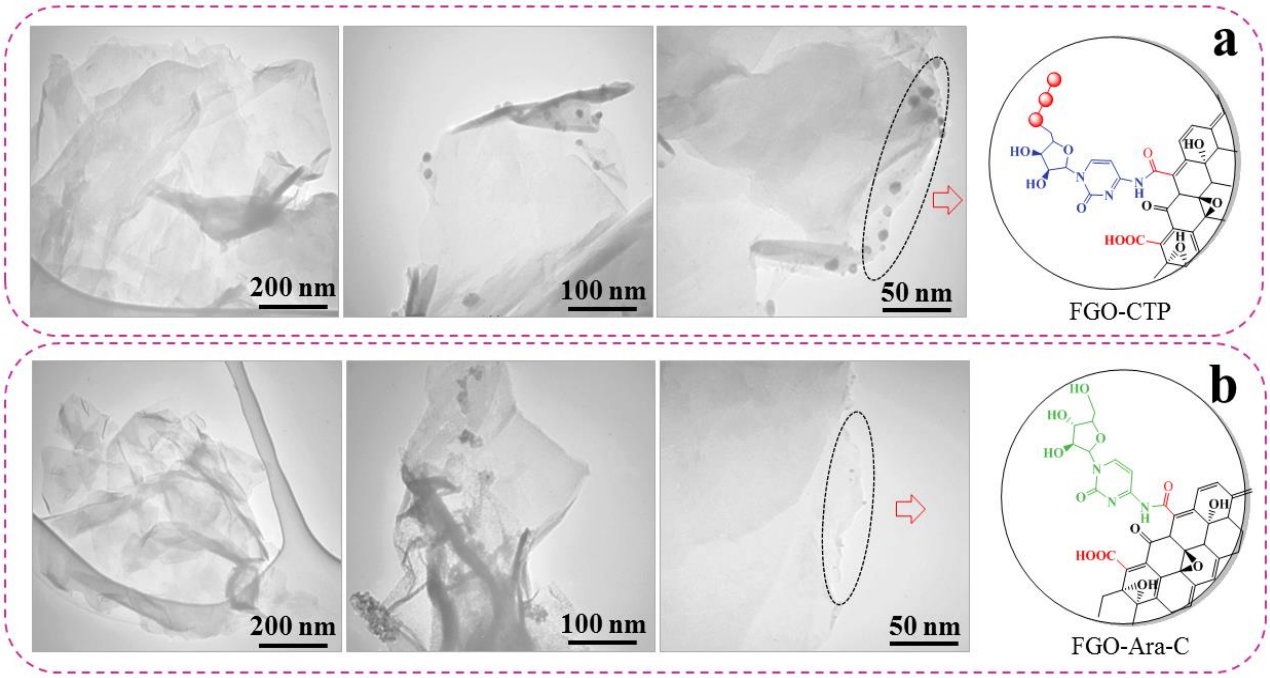

Fig. 5. TEM images of a) FGO-CTP and b) FGO-Ara-C.

FE-SEM is used as an effective approach to determine the morphology of material as it is considered for the impact of functionalization and accelerating factors on specific structures. The FE-SEM images of fabricated FGO-CTP and FGO-Ara-C composites can be seen in Fig. 4a and 4c. The average thickness of the pores ranges between 10µm and 500 nm. Besides, Energy Dispersive X-ray was introduced as a powerful tool to explain the distribution of atoms existing in different areas. Fig. 4b and 4c show the EDX of FGO-CTP and FGO-Ara-C and the approximate amount of atoms present in various areas, as calculated for carbon, nitrogen, oxygen, and phosphorous attributing effective functionalization applying the CTP and Ara-C groups[61,62]. In Fig. 5a and 5b, TEM images exhibit the electrons intensity attenuated by FGO-CTP and FGO-Ara-C platelet with the various thickness sizes. This indicates a sheet-like morphology with various transparencies of the examined area of about 200, 100, 50 nm. Dark areas show the thick stacking

nanostructure of several graphene oxides or graphene sheets with some oxygen functional groups[25].

5. Computational Results

We have started from the graphene primitive cell to create a single layer of graphene. Then we have constructed graphene oxide (GO) monolayer by adding different oxygen-containing functional groups to the graphene layer. Since the FT-IR results detected carboxylic and carbonyl groups mainly around the edges of the layer, we have constructed graphene oxide layer terminating with oxygen-containing functional groups of hydroxyl, carbonyl and carboxyl based on the Lerf-Klinowski [63] model.

Firstly, we constructed a unit cell of 31.68Å×21.37Å×34.81 Å with graphene monolayer at the middle where it is replicated into an infinite layer by periodic boundary condition. GO layer is then modelled by adding hydroxyl, carbonyl and carboxyl groups randomly around the edge and on the basal plane of graphene sheet, Fig. 6a. The supercell models of FGO-Ara-C and FGO-CTP used in our DFT calculations are shown in Fig.6b and 6c.

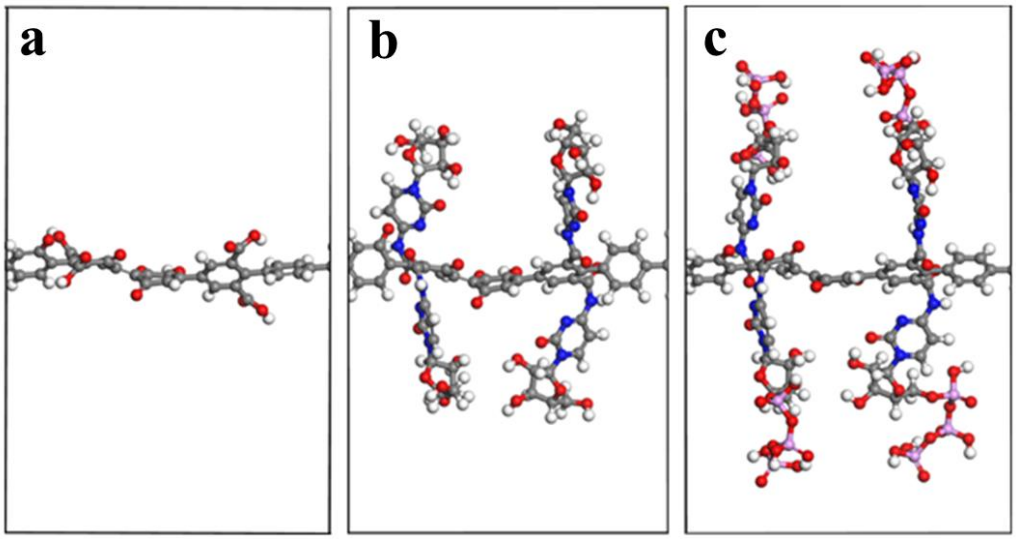

Fig. 6. Supercells view from side of the models of (a) GO monolayer (b) FGO-Ara-C and (c) FGO-CTP. Carbon atoms are shown in gray, oxygen atoms in red, nitrogen atoms in blue, phosphorus atoms in pink and hydrogen atoms in white spheres.

To gain more insight into the charge density distribution on GO layer of both FGO-Ara-C and FGO-CTP complexes, the topological analysis of electron density $\rho_{bcp}(r)$ and its Laplacian $\nabla^2_{\rho bc}\rho(r)$ at bonding critical points were carried out. The critical point search has been done for the (3, -1) type critical points of both complexes bonds. Fig. S2a shows the differences of electron density values of all bonds of C-C of GO layer in both FGO-Ara-C and FGO-CTP complexes, where the corresponding C-C bonds and their electron densities at the bcp's of all the C-C bonds are shown in Fig. S3 and Table S2 respectively. The electron densities $\rho_{bcp}(r)$ of most C-C bonds of GO layer are increased in FGO-CTP, which are attributed to the interactions of connected CTP to the GO layer. The average value of electron density $\rho_{bcp}(r)$ of C-C bonds of FGO-Ara-C and FGO-CTP are 2.007 and 2.009 $eÅ^{-3}$, respectively.

Similarly, the second derivative value of electron density ($\nabla^2_{\rho bc}\rho(r)$) at the bcp's is known as Laplacian reveals the nature of the bond, whether the bonding charges are concentrated or depleted. Fig. S2b and Table S2 show the differences of Laplacian charge densities in bcp' of C-C bonds of GO layer of FGO-Ara-C and FGO-CTP and their values, respectively. Fig. 7 and 8 show the $\nabla^2_{\rho bc}\rho(r)$ map of C-C bonds of GO layer of both compounds. It is well known that the positive and negative values of $\nabla^2_{\rho bc}\rho(r)$ correspond to charge depletion and concentration areas, respectively. The average $\nabla^2_{\rho bc}\rho(r)$ value for C-C bonds of GO layer are increased in FGO-CTP-C complex, where the values are -23.173 $eÅ^{-5}$ compared to -23.099 $eÅ^{-5}$ in FGO-Ara-C complex, confirming that the bond charges are more concentrated in FGO-CTP compound. As a result, on the basis of topological calculations done in this study, there is more charge distribution on FGO-CTP than that of FGO-Ara-C, which makes it more effective as an electrode material for supercapacitors.

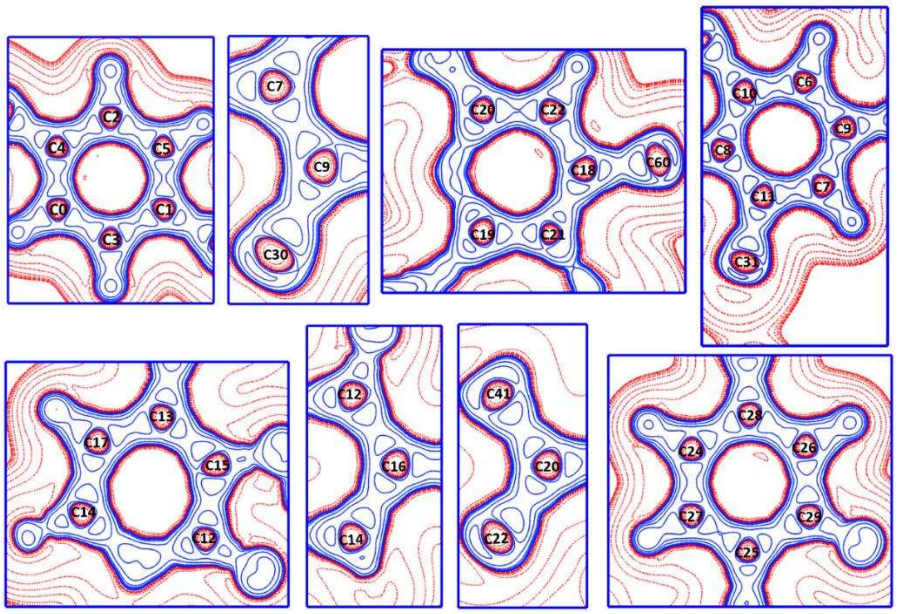

Fig. 7. The contour plot of Laplacian of electron density of GO layer of FGO-CTP obtained from DFT calculations. Contours are drawn in logarithmic scale, 3.0×2^N $eÅ^{-5}$, where N = 2, 4 and 8×10^n, n = -2, -1, 0, 1, 2. The blue solid lines represent positive contours and the red dotted lines represent negative contours.

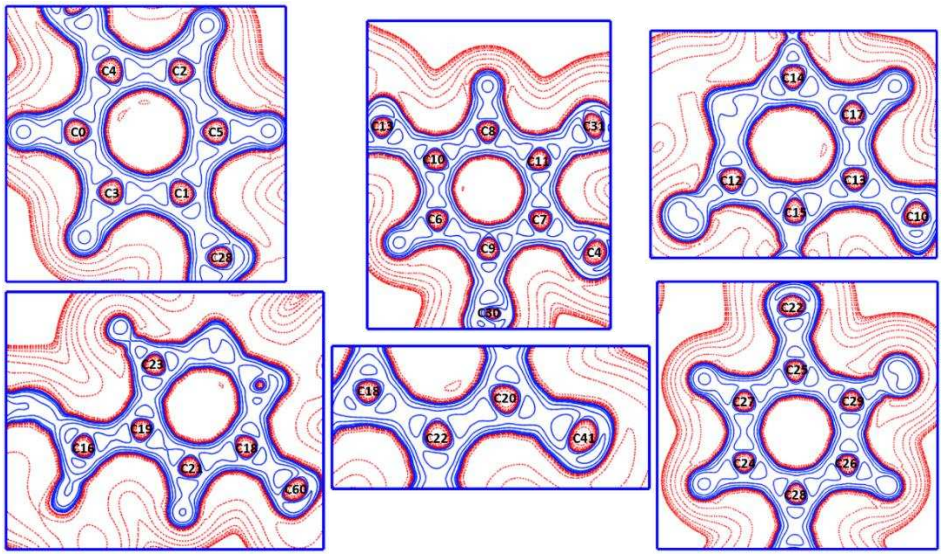

Fig. 8. The contour plot of Laplacian of electron density of GO layer of FGO-Ara-C obtained from DFT calculations. Contours are drawn in logarithmic scale, 3.0×2^N eÅ^{-5}, where N = 2, 4 and 8×10^n, n = -2, -1, 0, 1, 2. The blue solid lines represent positive contours and the red dotted lines represent negative contours.

6. Electrochemical Measurement

The reported CV curves were utilized in a three-electrode cell and 1M H_2SO_4 electrolyte solution for studying the supercapacitive behavior of the FGO-CTP and FGO-Ara-C electrodes at different rates of scanning (5 to 100 mV s^{-1}). As shown in Fig. 9a and 9b, the CV curves of FGO-CTP and FGO-Ara-C indicate a quasi-rectangular shape, confirming a notably pseudo-capacitive performance. Also, the CV curves of the FGO-CTP electrode are significantly greater than FGO-Ara-C, suggesting an increased active surface area for charge passing among the electrode and the electrolyte. The transfer of anodic and cathodic peaks to higher and lower potentials occurs with rising scan rates, which is owing to strong electrochemical polarization at higher rates of scan. Considering low scan rates, the electrons and ions of the electrolyte solution have sufficient time

to reach the reaction sites existing in electrode materials; but, at higher rates of scan, the charge shifting inside the materials is unable to keep up with the quick movement of electrons in the external circuit, resulting in electron collection on the electrode surface[64–68].As it can be seen in Fig 9c, in comparison, CV profiles of the FGO-CTP, FGO-Ara-C, and GO were calculated at a scan rate of 50 mV s^{-1} significantly. FGO-CTP, FGO-Ara-C, and GO displayed a valid potential range of -0.5 – 0.8 V, -0.4 – 0.6 V, and -0.4 – 0.6 V, respectively. Also, a rise in the number of scan rates resulted in FGO-CTP and FGO-Ara-C capacitance decreasing (Fig. 9d). The maximum capacitance values of 430 and 312 F g^{-1} were achieved for FGO-CTP and FGO-Ara-C at 5 mV s^{-1}, respectively.

Fig. S4 depicts the redox mechanism of samples. CTP molecules hydrolyze on the surface of graphene oxide and release $PO4^{-3}$ ions slowly, resulting in the development of a highly nanoporous structure enabling rapid electron transfer [69]. The oxygen functional groups have a significant impact on the capacitive efficiency of graphene oxide, as demonstrated in Fig. S4. Hydroxyl groups make a noticeable difference between FGO-CTP and FGO-Ara-C composites. Since the number of -OH groups of FGO-CTP was higher than that of FGO-Ara-C, the electrons on the oxygen functional groups were grabbed by H_3O^+ in the acidic aqueous electrolyte, leading to the separation of positive and negative charges and the occurrence of the redox process.The enhancement in capacity provided by oxygen functional groups may be assigned to many factors including the electrolyte's permeability on the graphene oxide surface had been improved, the Faraday pseudocapacitance supplied by electron transfer (redox reaction) could be provided, and the graphene oxide's pore utilization ratio would improve [70].

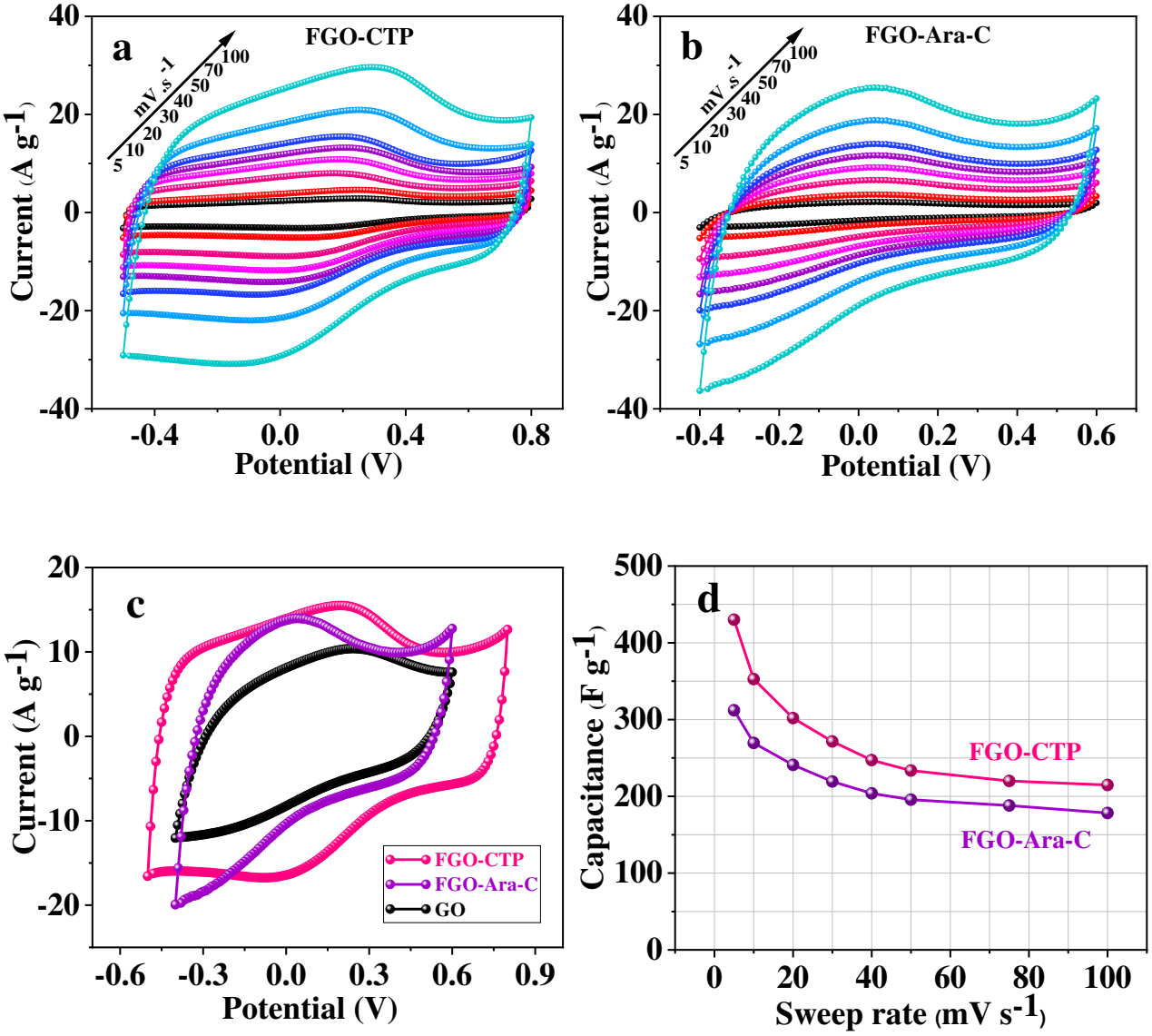

Fig. 9. Cyclic voltammograms a) FGO-CTP and b) FGO-Ara-C at incremental rates from 5 to 100 mV s^{-1}, c) cyclic voltammograms of the FGO-CTP, FGO-Ara-C, and GO at 50 mV s^{-1}, and d) special capacitance on the basis of the sweep rates for the FGO-CTP and FGO-Ara-C.

The GCD method was conducted for understanding the SC electrochemical properties. GCD diagrams are shown in Fig. 10a for two prepared materials at a current density of 1 A g^{-1}, which are triangular, linear symmetrical, and relatively sharp. Also, the equilateral triangle structure of

the FGO-CTP and FGO-Ara-C electrodes suggests an effective capacitive performance and good reversibility during the GCD process[71–73]. Fig. S5a and S5b show GCD plots of FGO-CTP and FGO-Ara-C electrodes at different current densities between 0.5 - 16 A g^{-1}. Furthermore, the reversible performance, elevated columbic efficiency, and excellent capacitor behavior of samples is the probable result of the equivalent durations of charge and discharge. According to discharge curves, Equation 1 is reported for the calculation of specific capacitance[74–78]:

$$C = \frac{I\,\Delta t}{\Delta V\,m} \qquad (1)$$

Where I, Δt, and ΔV respectively show discharge current (A), total time (s), and potential change (V), and m devotes the total mass of the electroactive material (g). Fig. 10b displays the approximate specific capacitance as a function of the current discharge density varying from 0.5 - 16 A g^{-1}. Actually, by increasing the current density values, the corresponding capacitances are decreasing. The specific capacitances of 375, 269, and 97 F g^{-1} reached for FGO-CTP, FGO-Ara-C, and GO electrodes, respectively, at 1 A g^{-1}. These findings reveal higher accessible electroactive sites in the FGO-CTP electrode in comparison with its competitor. The measured capacitance retention was plotted versus the cycle numbers for FGO-CTP and FGO-Ara-C at 8 A g^{-1} (Fig. 10c). The reduction in capacitance happened following 5000 continuous cycles at 8 A g^{-1} remaining values of 92.3 and 89.4% for FGO-CTP and FGO-Ara-C, respectively.

The significant improvement in FGO-CTP electrochemical performance can be assigned to the presence of the CTP groups for providing better supercapacitive behavior to graphene oxide compared to the Ara-C ligand. Furthermore, the scientific data and measured cycling stability derived from GCD plots strongly support the CV results. According to the achieved electrochemical results in a three-electrode configuration, the FGO-CTP electrode exhibited higher

capacitance, cycling stability, and ionic conductivity compared to the FGO-Ara-C electrode. Table. 1. indicates the SC behavior of fabricated electrodes compared to other reported materials.

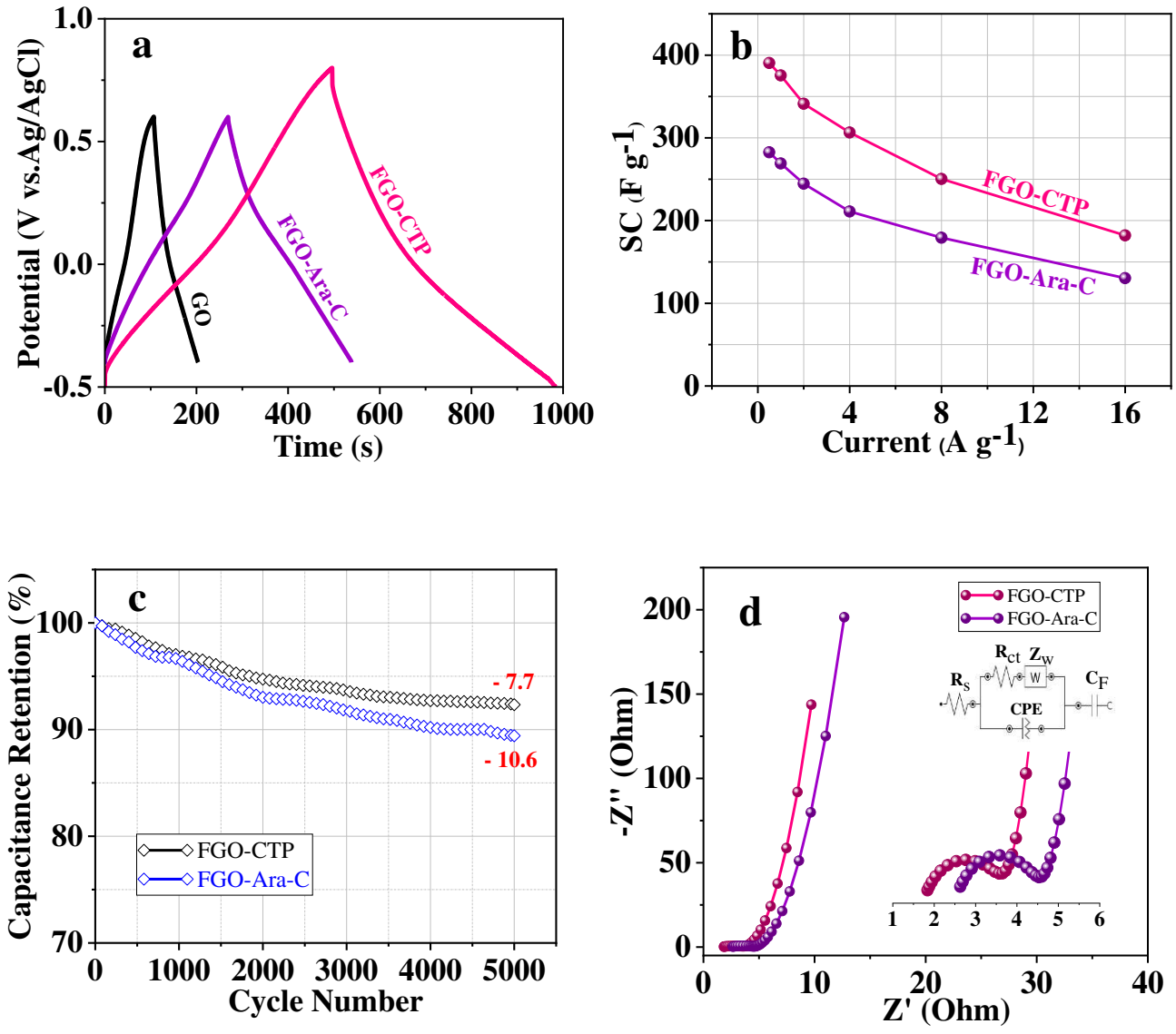

Fig. 10. a) GCD curves of FGO-CTP, FGO-Ara-C, and GO at 1 A g^{-1}, b) Variation of SC vs. current density, c) The cycling stability of the FGO-CTP and FGO-Ara-C at 8 A g^{-1}, and d) Nyquist plots of the FGO-CTP and FGO-Ara-C electrodes.

Table. 1. Different values of specific capacitance, cycling stability, and electrolyte for graphene based electrodes.

Electrode	Electrolyte	Specific capacitance	Measurement condition	Cycling stability	Reference
BHGO	1M H_2SO_4	170 F g^{-1}	1 A g^{-1}	85% over 5000 cycles	[79]
COF/rGO	0.5M H_2SO_4	269 F g^{-1}	0.5 A g^{-1}	96% over 5000 cycles	[80]
NrGO/GQD	6M KOH	344 F g^{-1}	0.25 A g^{-1}	82% over 3000 cycles	[81]
NG	6M KOH	225.2 F g^{-1}	1 A g^{-1}	90% over 5000 cycles	[82]
MnO_2/rEGO	6M KOH	342.8 F g^{-1}	0.5 A g^{-1}	90.3% over 3000 cycles	[83]
GO-bis(PIEA)	6M KOH	287 F g^{-1}	1 A g^{-1}	95 % over 1000 cycles	[84]
FGO-TBpa	6M KOH	305 F g^{-1}	1 A g^{-1}	90% over 1000 cycles	[85]
POA/CNT/rGO	1M H_2SO_4	274.9 F g^{-1}	1 A g^{-1}	93% over 500 cycles	[86]
BRGO /MWCNT-Fe_3O_4	1M KOH	167 F g^{-1}	1 A g^{-1}	94% over 1000 cycles	[87]
DMFrGO180	PVA/KOH gel	287 F g^{-1}	1 A g^{-1}	73.8% over 5000 cycles	[88]
FGO-CTP	**1M H_2SO_4**	**430 F g^{-1}**	**1 A g^{-1}**	**92.3% over 5000 cycles**	**This Work**
FGO-Ara-C	**1M H_2SO_4**	**312 F g^{-1}**	**1 A g^{-1}**	**89.4% over 5000 cycles**	**This Work**

In order to evaluate the internal charging processes that emerged between the electrolyte and the electrode, the EIS technique was used with a 0 V potential in the frequency range of 0.01 Hz to 100 kHz. Fig. 10d shows the Nyquist plots of FGO-CTP and FGO-Ara-C electrodes. As indicated in the diagram, the plots describe the electrodes with small semicircles in a broad frequency region due to the charge transferring between the electrode and the electrolyte. EIS spectrum fitting was performed using the equivalent circuit. Supercapacitors behave as a resistor at large frequencies

where the interception at the real axis area shows equivalent series resistance like electrolyte resistance, substrate's Intrinsic resistance, and interaction resistance between the interface of the current collector and the active material[89–94].

EIS technique includes the constant phase element (CPE) applied as a double-layer capacitance (C_{dl}), charge transfer (R_{ct}), resistance to bulk solution (R_s), Warburg resistance (Z_w), and a faradaic capacitance (C_F) in the FGO-CTP and FGO-Ara-C electrodes. In Table. 2, optimized R_s, Z_w, CPE, R_{ct}, and C_F values after complex nonlinear least square (CNLS) fitting are shown, confirming higher electrochemical efficiency of FGO-CTP than FGO-Ara-C electrode. R_s of FGO-CTP and FGO-Ara-C was calculated to be 1.88 and 2.52 Ω, respectively, while R_{ct} was measured to be 1.77 and 2.01 Ω, respectively. The low R_{ct} values of as-prepared electrodes signified simpler electrochemical reactions at the electrode/electrolyte interface. C_F values of FGO-CTP and FGO-Ara-C electrodes were obtained 115.46 and 84.91 mF, respectively. Also, Z_W, which shows the ion diffusion/transport frequency activity[95] to the surface of the electrode in the form of straight lines, is calculated to be 0.47 and 0.34 for FGO-CTP and FGO-Ara-C electrodes, respectively. As Shown in Fig. 10d, the FGO-CTP electrode demonstrates a larger value of Warburg resistance than that of FGO-Ara-C, proving the higher length of diffusion route for ions transports. To conclude, as shown in Table 2, the graphene oxide functionalized with the CTP group showed an enhanced electrochemical behavior as compared to the FGO-Ara-C electrode.

Table. 2. The measured values of R_S, CPE, Z_W, R_{ct}, and C_F through CNLS fit the spectrum of experimental impedance based on the proposed equivalent circuit.

	R_s (Ω)	**CPE-Y0 (mF)**	**CPE-N**	**Z_w**	**R_{ct} (Ω)**	**C_F (mF)**

FGO-CTP	1.88	1.56	0.79	0.47	1.77	115.46
FGO-Ara-C	2.52	0.74	0.77	0.34	2.01	84.91

7. Symmetric Performance of the FGO-CTP//FGO-CTP and FGO-Ara-C//FGO-Ara-C electrodes

The electrochemical behavior of the FGO-CTP and FGO-Ara-C was also studied in a SSC cell configuration applying 1M H_2SO_4 electrolyte. Standard CV curve shapes range between 0 to 1.3 and 0 to 1 V for FGO-CTP//FGO-CTP and FGO-Ara-C//FGO-Ara-C, respectively. Fig. 11a and 11b show the CV curves of the symmetrical systems at various sweep rates (5-100 mV s^{-1}). When employed sweep rate enhanced, the potential window exhibited a more considerable background. Moreover, a quasi-reversible electron shifting mechanism takes place in the CV curves of electrodes, showing that the enhanced capacitance was associated with the ideal activity of the redox process[96–98]. As depicted in Fig. 11c, voltammograms for the FGO-CTP//FGO-CTP and FGO-Ara-C//FGO-Ara-C are compared at the scan rate of 50 mV s^{-1}. As a result of this comparison and according to the pseudocapacitance arising from the oxidation/reduction reactions that occurred in the positive electrode, the FGO-CTP//FGO-CTP delivers a greater capacitance than the FGO-Ara-C//FGO-Ara-C at the same scan rate. The variations of SC as a function of sweep rate is also indicated in Fig. 11d. Specific capacitances of 212 and 150 F g^{-1} were achieved for cells containing FGO-CTP//FGO-CTP and FGO-Ara-C//FGO-Ara-C at 5 mv s^{-1}.

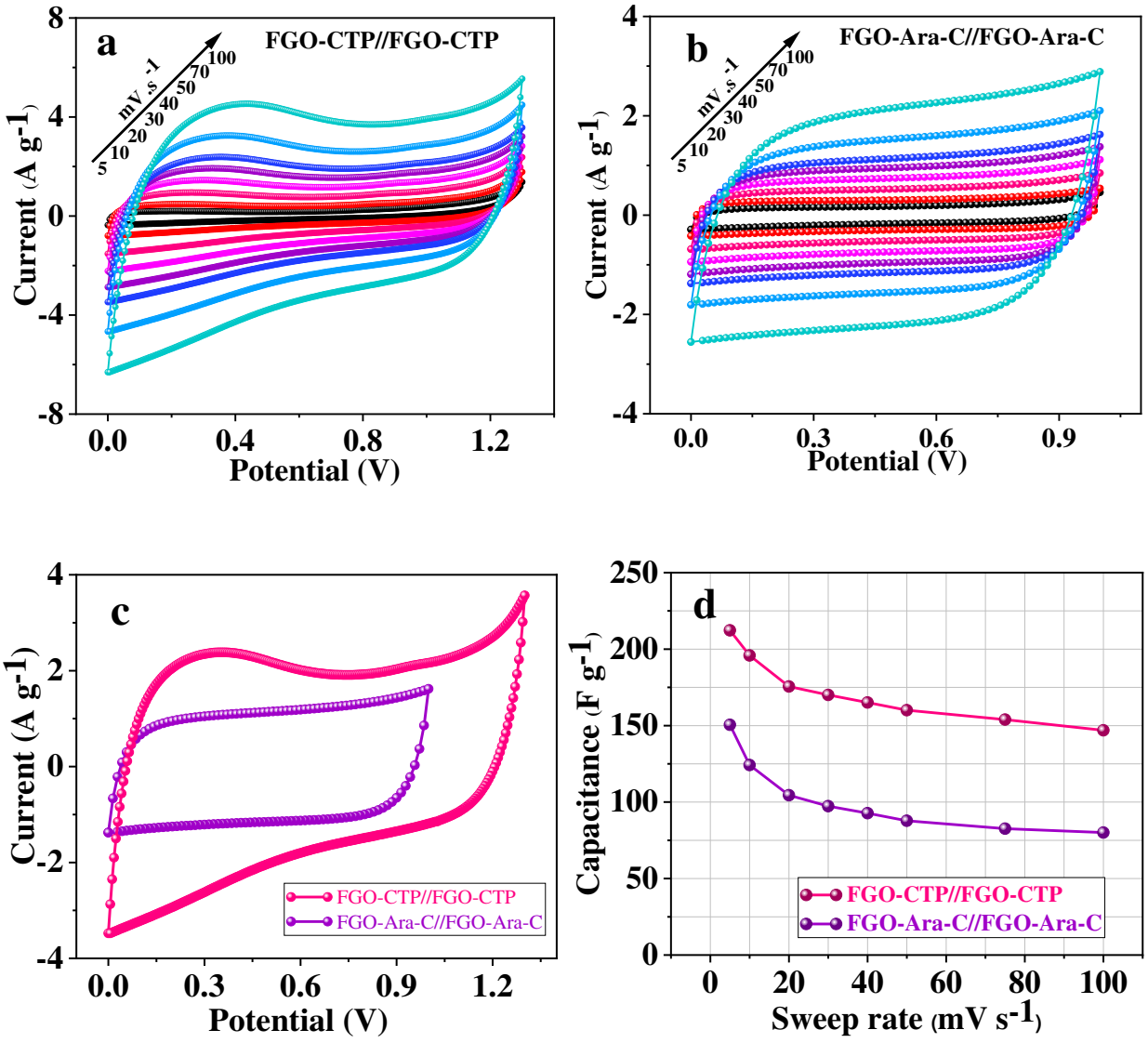

Fig. 11. CV curves at different scan rates of a) FGO-CTP//FGO-CTP, b) FGO-Ara-C//FGO-Ara-C; c) Comparison of the voltammograms of FGO-CTP//FGO-CTP and FGO-Ara-C//FGO-Ara-C, and d) special capacitance on the basis of the sweep rates for the FGO-CTP//FGO-CTP and FGO-Ara-C//FGO-Ara-C supercapacitors in symmetric configurations.

Charge/discharge curves diagrams of FGO-CTP//FGO-CTP and FGO-Ara-C//FGO-Ara-C devices are shown in Fig. 12a at 1 A g^{-1} and the voltage ranges are presented in the CV part. Also, in Fig.

S5c and S5d, GCD diagrams for two prepared electrodes at different current densities are exhibited. When examined at different current densities, these figures exhibit reasonably symmetric forms, demonstrating their remarkable supercapacitive nature. Specific capacitance for one electrode may be calculated by equation 2[99]:

$$C_{electrode} = \frac{4\ C_{device}}{m} \qquad (2)$$

where C_{device} is the measured capacitance for the two-electrode cell and *m* is the active materials' total mass in both electrodes. In Fig. 12b, The SC plots versus current density are shown. Specific capacitances of 194 and 126 F g^{-1} were achieved for the cell, including the FGO-CTP//FGO-CTP and FGO-Ara-C//FGO-Ara-C at 1 A g^{-1}. As depicted in Fig. 12c, during the charge or discharge reaction, the FGO-CTP//FGO-CTP configuration represented superior cyclic stability (94.5%) compared to FGO-Ara-C//FGO-Ara-C (91.3%) over 5000 cycles at 8 A g^{-1}.

Moreover, the energy density (E_d) and power density (P_d) of the FGO-CTP//FGO-CTP and FGO-Ara-C//FGO-Ara-C symmetric supercapacitor are presented in the Ragone graph (Fig. 12d). The values of E_d and P_d were accordingly achieved on the basis of Equations 3 and 4 for additional electrochemical studies, respectively[99–101].

$$E_d(W\ h\ Kg^{-1}) = \frac{1}{7.2}\ C_{device}\ .\Delta V^2 \qquad (3)$$

$$P_d(W\ Kg^{-1}) = \frac{E_d \times 3600}{\Delta t} \qquad (4)$$

The FGO-CTP//FGO-CTP and FGO-Ara-C//FGO-Ara-C demonstrate E_d value of 17.8 and 6.9 W h Kg^{-1} at 325 and 250 W kg^{-1}, which is superior than some previously reported energy storage devices, such as POA/CNT/rGO (12.6 Wh kg^{-1} at 276.6 W kg^{-1})[86], DMFrGO180 (11.35 Wh kg^{-1} at 649.7 W kg^{-1})[88] and MGA (17.8 Wh kg^{-1} at 400 W kg^{-1})[102].

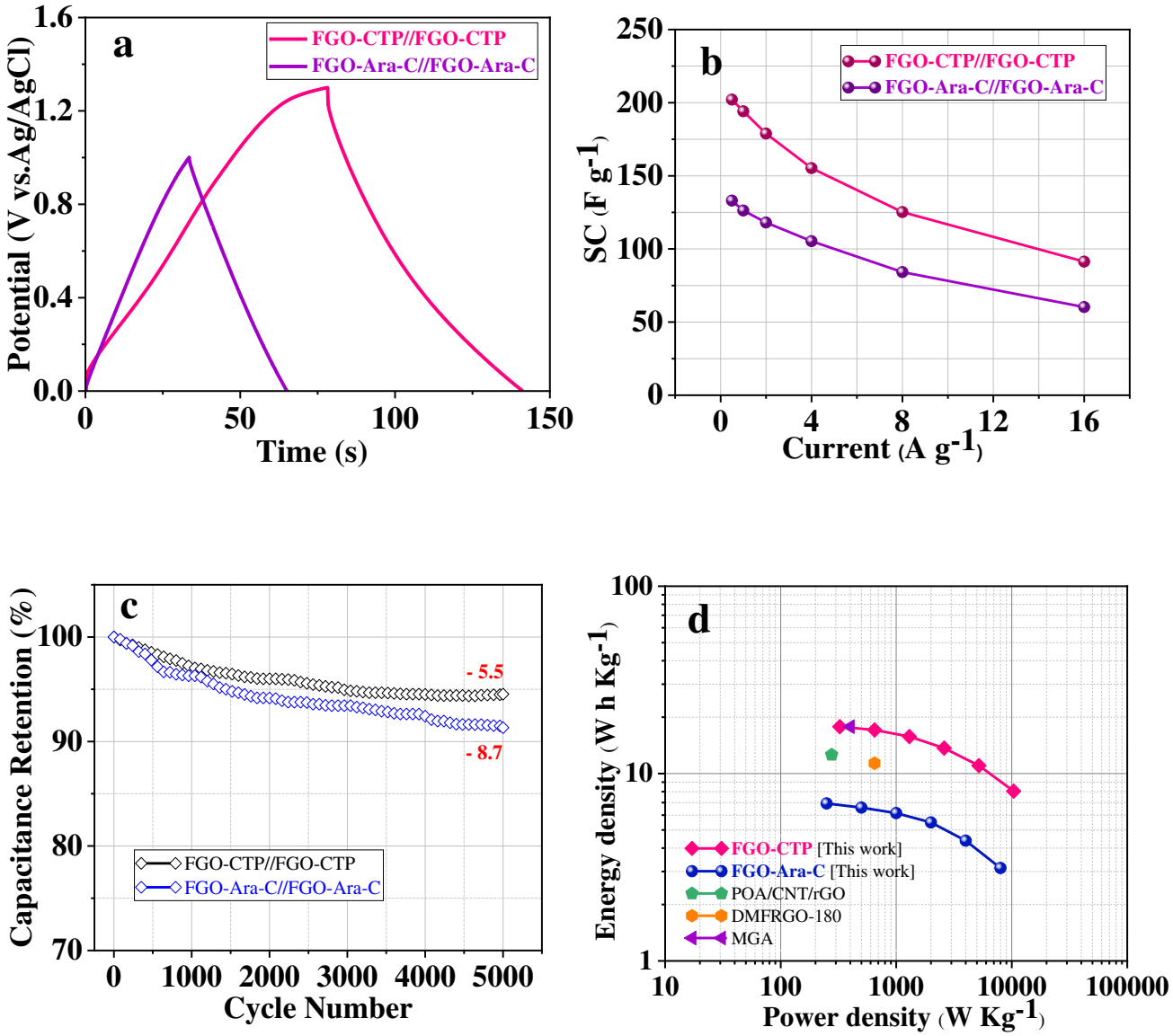

Fig. 12. a) GCD curves of FGO-CTP//FGO-CTP and FGO-Ara-C//FGO-Ara-C at 1 A g^{-1}; b) variations of SC as a function of current density c) cycle performance of FGO-CTP//FGO-CTP and FGO-Ara-C//FGO-Ara-C electrodes at a current density of 8 A g^{-1}; d) ragone plot of the FGO-CTP//FGO-CTP and FGO-Ara-C//FGO-Ara-C.

8. Conclusion

In this study, the functionalized graphene oxides (FGO-CTP and FGO-Ara-C) were prepared by a chemically synthesized approach and validated by different analytical methods such as XPS, FT-IR, XRD, and Raman characterizations. The main role of CTP molecules in FGO-CTP is releasing PO_4^{-3} ions via hydrolyzing on the surface of GO leading to the construction of a high surface area structure for fast electron transfer. The as-prepared composite of FGO-CTP revealed a specific capacitance of 430 F g^{-1} at 5 mV s^{-1} than that of FGO-Ara-C (312 F g^{-1}) within a three-electrode cell. More noticeably, for symmetric configuration, FGO-CTP//FGO-CTP showed greater capacitance of 212 F g^{-1} at 5 mV s^{-1} and good retention capacity as high as 94.5% in a 1M H_2SO_4 electrolyte. Also, the energy density of 17.8 Wh kg^{-1} at a power density of 325 W kg^{-1} was obtained for the FGO-CTP//FGO-CTP device. Topological analysis of electron density and its Laplacian confirmed more charge density distribution on GO layer of FGO-CTP. These impressive results make energy storage devices a promising candidate for further research and practical applications.

Acknowledgment

The authors would like to gratefully thank the Research Affairs Division of the Amirkabir University of Technology (AUT), Tehran, Iran, for their financial support. This work has used the computational facilities of the Advanced Research Computing at Cardiff (ARCCA) Division, Cardiff University, and HPC Wales.

References

[1] Z. Zhang, F. Xiao, L. Qian, J. Xiao, S. Wang, Y. Liu, Facile synthesis of 3D MnO2-graphene and carbon nanotube-graphene composite networks for high-performance, flexible, all-solid-state asymmetric supercapacitors, Adv. Energy Mater. 4 (2014)

1400064. https://doi.org/10.1002/aenm.201400064.

[2] Z. Liu, H. Zhang, Q. Yang, Y. Chen, Graphene / V2O5 hybrid electrode for an asymmetric supercapacitor with high energy density in an organic electrolyte, Electrochim. Acta. 287 (2018) 149–157. https://doi.org/10.1016/j.electacta.2018.04.212.

[3] D.J. Ahirrao, K. Mohanapriya, N. Jha, V2O5 nanowires-graphene composite as an outstanding electrode material for high electrochemical performance and long-cycle-life supercapacitor, Mater. Res. Bull. 108 (2018) 73–82. https://doi.org/10.1016/j.materresbull.2018.08.028.

[4] D.D.L. Chung, Development, design and applications of structural capacitors, Appl. Energy. 231 (2018) 89–101. https://doi.org/10.1016/j.apenergy.2018.09.132.

[5] L.L. Zhang, R. Zhou, X.S. Zhao, Graphene-based materials as supercapacitor electrodes, J. Mater. Chem. 20 (2010) 5983–5992. https://doi.org/10.1039/c000417k.

[6] Z. Shen, J. Du, Y. Mo, A. Chen, Nanocomposites of reduced graphene oxide modified with mesoporous carbon layers anchored by hollow carbon spheres for energy storage, Carbon N. Y. 173 (2021) 22–30. https://doi.org/10.1016/j.carbon.2020.10.087.

[7] S.E.M. Pourhosseini, O. Norouzi, P. Salimi, H.R. Naderi, Synthesis of a Novel Interconnected 3D Pore Network Algal Biochar Constituting Iron Nanoparticles Derived from a Harmful Marine Biomass as High-Performance Asymmetric Supercapacitor Electrodes, ACS Sustain. Chem. Eng. 6 (2018) 4746–4758. https://doi.org/10.1021/acssuschemeng.7b03871.

[8] Q. Chang, L. Li, L. Sai, W. Shi, Q. Chen, L. Huang, Interconnected binary carbon hybrids for supercapacitor electrode, Electrochim. Acta. 251 (2017) 293–300. https://doi.org/10.1016/j.electacta.2017.08.109.

[9] X. Bing, Y. Wei, M. Wang, S. Xu, D. Long, J. Wang, W. Qiao, L. Ling, Template-free synthesis of nitrogen-doped hierarchical porous carbons for CO2 adsorption and supercapacitor electrodes, J. Colloid Interface Sci. 488 (2017) 207–217. https://doi.org/10.1016/j.jcis.2016.10.076.

[10] C.M. Chen, Q. Zhang, X.C. Zhao, B. Zhang, Q.Q. Kong, M.G. Yang, Q.H. Yang, M.Z. Wang, Y.G. Yang, R. Schlögl, D.S. Su, Hierarchically aminated graphene honeycombs for electrochemical capacitive energy storage, J. Mater. Chem. 22 (2012) 14076–14084. https://doi.org/10.1039/c2jm31426f.

[11] G. Sharma, A. Kumar, M. Naushad, S. Sharma, A.A. Ghfar, T. Ahamad, C. Si, F.J. Stadler, Graphene oxide supported La/Co/Ni trimetallic nano-scale systems for photocatalytic remediation of 2-chlorophenol, J. Mol. Liq. 294 (2019) 111605. https://doi.org/10.1016/j.molliq.2019.111605.

[12] A.A. Novikova, V.E. Burlakova, V.N. Varavka, I.E. Uflyand, E.G. Drogan, V.A. Irkha, Influence of glycerol dispersions of graphene oxide on the friction of rough steel surfaces, J. Mol. Liq. 284 (2019) 1–11. https://doi.org/10.1016/j.molliq.2019.03.111.

[13] G. Abdi, A. Alizadeh, J. Amirian, S. Rezaei, G. Sharma, Polyamine-modified magnetic graphene oxide surface: Feasible adsorbent for removal of dyes, J. Mol. Liq. 289 (2019)

111118. https://doi.org/10.1016/j.molliq.2019.111118.

[14] V.P. Chauke, A. Maity, A. Chetty, High-performance towards removal of toxic hexavalent chromium from aqueous solution using graphene oxide-alpha cyclodextrin-polypyrrole nanocomposites, J. Mol. Liq. 211 (2015) 71–77. https://doi.org/10.1016/j.molliq.2015.06.044.

[15] S.K. Shinde, S. Ramesh, C. Bathula, G.S. Ghodake, D.-Y. Kim, A.D. Jagadale, A.A. Kadam, D.P. Waghmode, T.V.M. Sreekanth, H.S. Kim, P.C. Nagajyothi, H.M. Yadav, Novel approach to synthesize NiCo2S4 composite for high-performance supercapacitor application with different molar ratio of Ni and Co, Sci. Rep. 9 (2019) 13717. https://doi.org/10.1038/s41598-019-50165-5.

[16] S.K. Shinde, M.B. Jalak, G.S. Ghodake, N.C. Maile, V.S. Kumbhar, D.S. Lee, V.J. Fulari, D.-Y. Kim, Chemically synthesized nanoflakes-like NiCo2S4 electrodes for high-performance supercapacitor application, Appl. Surf. Sci. 466 (2019) 822–829. https://doi.org/10.1016/j.apsusc.2018.10.100.

[17] N. Kumar, A.T. Kozakov, A.V. Sidashov, A.V. Nicolskii, Tribofilm stability of ionic liquid functionalized graphene-oxide in metallic contact interfaces, J. Mol. Liq. 296 (2019) 111813. https://doi.org/10.1016/j.molliq.2019.111813.

[18] A. Jamsaz, E.K. Goharshadi, Flame retardant, superhydrophobic, and superoleophilic reduced graphene oxide/orthoaminophenol polyurethane sponge for efficient oil/water separation, J. Mol. Liq. 307 (2020) 112979. https://doi.org/10.1016/j.molliq.2020.112979.

[19] G. Yang, N. Song, F. Deng, J. Liang, Q. Huang, J. Dou, Y. Wen, M. Liu, X. Zhang, Y. Wei, Direct surface functionalization of graphene oxide with ionic liquid through gamma ray irradiation induced radical polymerization with remarkable enhanced adsorption capacity, J. Mol. Liq. 306 (2020) 112877. https://doi.org/10.1016/j.molliq.2020.112877.

[20] A.S.K. Kumar, S.-J. Jiang, Synthesis of magnetically separable and recyclable magnetic nanoparticles decorated with β-cyclodextrin functionalized graphene oxide an excellent adsorption of As(V)/(III), J. Mol. Liq. 237 (2017) 387–401. https://doi.org/10.1016/j.molliq.2017.04.093.

[21] J.S. Shayeh, S.O.R. Siadat, M. Sadeghnia, K. Niknam, M. Rezaei, N. Aghamohammadi, Advanced studies of coupled conductive polymer/metal oxide nano wire composite as an efficient supercapacitor by common and fast fourier electrochemical methods, J. Mol. Liq. 220 (2016) 489–494. https://doi.org/10.1016/j.molliq.2016.04.122.

[22] R. Thangappan, M. Arivanandhan, R. Dhinesh Kumar, R. Jayavel, Facile synthesis of RuO2 nanoparticles anchored on graphene nanosheets for high performance composite electrode for supercapacitor applications, J. Phys. Chem. Solids. 121 (2018) 339–349. https://doi.org/10.1016/j.jpcs.2018.05.049.

[23] K. Kemp, J. Griffiths, S. Campbell, K. Lovell, An exploration of the follow-up up needs of patients with inflammatory bowel disease, J. Crohn's Colitis. 7 (2013) e386–e395. https://doi.org/10.1016/j.crohns.2013.03.001.

[24] S. Mondal, U. Rana, S. Malik, Reduced Graphene Oxide/Fe3O4/Polyaniline

Nanostructures as Electrode Materials for an All-Solid-State Hybrid Supercapacitor, J. Phys. Chem. C. 121 (2017) 7573–7583. https://doi.org/10.1021/acs.jpcc.6b10978.

[25] F.B. Ajdari, E. Kowsari, H.R. Nadri, M. Maghsoodi, A. Ehsani, H. Mahmoudi, S.K. Eshkalak, A. Chinnappan, W.A.D.M. Jayathilak, S. Ramakrishna, Electrochemical performance of Silsesquioxane-GO loaded with alkoxy substituted ammonium-based ionic liquid and POAP for supercapacitor, Electrochim. Acta. 354 (2020) 136663. https://doi.org/10.1016/j.electacta.2020.136663.

[26] S. Lin, J. Tang, K. Zhang, T.S. Suzuki, Q. Wei, M. Mukaida, Y. Zhang, H. Mamiya, X. Yu, L.C. Qin, High-rate supercapacitor using magnetically aligned graphene, J. Power Sources. 482 (2021) 228995. https://doi.org/10.1016/j.jpowsour.2020.228995.

[27] J. Yan, Z. Fan, T. Wei, W. Qian, M. Zhang, F. Wei, Fast and reversible surface redox reaction of graphene-MnO2 composites as supercapacitor electrodes, Carbon N. Y. 48 (2010) 3825–3833. https://doi.org/10.1016/j.carbon.2010.06.047.

[28] Z. Yu, M. McInnis, J. Calderon, S. Seal, L. Zhai, J. Thomas, Functionalized graphene aerogel composites for high-performance asymmetric supercapacitors, Nano Energy. 11 (2015) 611–620. https://doi.org/10.1016/j.nanoen.2014.11.030.

[29] S.P. Lee, G.A.M. Ali, H. Algarni, K.F. Chong, Flake size-dependent adsorption of graphene oxide aerogel, J. Mol. Liq. 277 (2019) 175–180. https://doi.org/10.1016/j.molliq.2018.12.097.

[30] Y.M.Y. Albarqouni, S.P. Lee, G.A.M. Ali, A.S. Ethiraj, H. Algarni, K.F. Chong, Facile synthesis of reduced graphene oxide aerogel in soft drink as supercapacitor electrode, J. Nanostructure Chem. (2021) 1–11. https://doi.org/10.1007/s40097-021-00424-7.

[31] W.S. Hummers, R.E. Offeman, Preparation of Graphitic Oxide, J. Am. Chem. Soc. 80 (1958) 1339. https://doi.org/10.1021/ja01539a017.

[32] E. Kowsari, A. Ehsani, M. Dashti Najafi, M. Bigdeloo, Enhancement of pseudocapacitance performance of p-type conductive polymer in the presence of newly synthesized graphene oxide-hexamethylene tributylammonium iodide nanosheets, J. Colloid Interface Sci. 512 (2018) 346–352. https://doi.org/10.1016/j.jcis.2017.10.076.

[33] M.D. Najafi, E. Kowsari, H.R. Naderi, A. Chinnappan, S. Ramakrishna, A. Ehsani, A. Shokravi, Functionalization of graphene oxide via chromium complexes coordinated on 5-aminopyridine-2-carboxylic acid as a symmetric supercapacitor electrode materials in energy storage devices, Compos. Sci. Technol. 211 (2021) 108844. https://doi.org/10.1016/j.compscitech.2021.108844.

[34] R. Nityananda, P. Hohenberg, W. Kohn, Inhomogeneous electron gas, Resonance. 22 (2017) 809–811. https://doi.org/10.1007/s12045-017-0529-3.

[35] W. Kohn, L.J. Sham, Self-consistent equations including exchange and correlation effects, Phys. Rev. 140 (1965) A1133. https://doi.org/10.1103/PhysRev.140.A1133.

[36] A.D. Becke, A new mixing of Hartree-Fock and local density-functional theories, J. Chem. Phys. 98 (1993) 1372–1377. https://doi.org/10.1063/1.464304.

[37] G. Kresse, J. Furthmüller, Efficiency of ab-initio total energy calculations for metals and semiconductors using a plane-wave basis set, Comput. Mater. Sci. 6 (1996) 15–50. https://doi.org/10.1016/0927-0256(96)00008-0.

[38] G. Kresse, J. Furthmüller, Efficient iterative schemes for ab initio total-energy calculations using a plane-wave basis set, Phys. Rev. B - Condens. Matter Mater. Phys. 54 (1996) 11169–11186. https://doi.org/10.1103/PhysRevB.54.11169.

[39] P.E. Blöchl, Projector augmented-wave method, Phys. Rev. B. 50 (1994) 17953–17979. https://doi.org/10.1103/PhysRevB.50.17953.

[40] S. Grimme, S. Ehrlich, L. Goerigk, Effect of the damping function in dispersion corrected density functional theory, J. Comput. Chem. 32 (2011) 1456–1465. https://doi.org/10.1002/jcc.21759.

[41] J.D. Pack, H.J. Monkhorst, "special points for Brillouin-zone integrations"-a reply, Phys. Rev. B. 16 (1977) 1748–1749. https://doi.org/10.1103/PhysRevB.16.1748.

[42] S. Abdpour, E. Kowsari, B. Bazri, M.R.A. Moghaddam, S.S. Tafreshi, N.H. de Leeuw, I. Simon, L. Schmolke, D. Dietrich, S. Ramakrishna, C. Janiak, Amino-functionalized MIL-101(Cr) photodegradation enhancement by sulfur-enriched copper sulfide nanoparticles: An experimental and DFT study, J. Mol. Liq. 319 (2020) 114341. https://doi.org/10.1016/j.molliq.2020.114341.

[43] C.F. Matta, R.J. Boyd, The Quantum Theory of Atoms in Molecules: From Solid State to DNA and Drug Design, Quantum Theory Atoms Mol. From Solid State to DNA Drug Des. (2007) 1–527. https://doi.org/10.1002/9783527610709.

[44] R.F.W. Bader, Atoms in Molecules, Prentice Hall Manchester, 1985. https://doi.org/10.1021/ar00109a003.

[45] R.F.W. Bader, Atoms in Molecules: A Quantum Theory, International Series of Monographs on Chemistry 22, Oxford Univ. Press. Oxford Henkelman G, Arnaldsson A, Jónsson H A Fast Robust Algorithm Bader Decompos. Charg. Density. Comput Mater Sci. 36 (1990) 354–360.

[46] D. Vega, D. Almeida, AIM-UC: An application for QTAIM analysis, J. Comput. Methods Sci. Eng. 14 (2014) 131–136. https://doi.org/10.3233/JCM-140491.

[47] M. Mohamadi, E. Kowsari, V. haddadi-Asl, M. Yousefzadeh, A. Chinnappan, S. Ramakrishna, Highly-efficient microwave absorptivity in reduced graphene oxide modified with PTA@ imidazolium based dicationic ionic liquid and fluorine atom, Compos. Sci. Technol. 188 (2020) 107960. https://doi.org/10.1016/j.compscitech.2019.107960.

[48] B. Peng, Y. Xu, K. Liu, X. Wang, F.M. Mulder, High-Performance and Low-Cost Sodium-Ion Anode Based on a Facile Black Phosphorus−Carbon Nanocomposite, ChemElectroChem. 4 (2017) 2140–2144. https://doi.org/10.1002/celc.201700345.

[49] B. Peng, Y. Xu, K. Liu, X. Wang, F.M. Mulder, High-Performance and Low-Cost Sodium-Ion Anode Based on a Facile Black Phosphorus−Carbon Nanocomposite, ChemElectroChem. 4 (2017) 2140–2144. https://doi.org/10.1002/celc.201700345.

[50] E. Kowsari, F. Morad, N. Seifvand, B. Bazri, M. Karimi, Synthesis of reduced graphene oxide functionalized with methyl red dye and its role in enhancing photoactivity in TiO2–IL/WO3 composite for toluene degradation, Res. Chem. Intermed. 46 (2020) 1217–1234. https://doi.org/10.1007/s11164-019-04030-9.

[51] B.D. Ossonon, D. Bélanger, Synthesis and characterization of sulfophenyl-functionalized reduced graphene oxide sheets, RSC Adv. 7 (2017) 27224–27234. https://doi.org/10.1039/c6ra28311j.

[52] H.D. Hanoon, E. Kowsari, M. Abdouss, H. Zandi, M.H. Ghasemi, Efficient preparation of acidic ionic liquid-functionalized reduced graphene oxide and its catalytic performance in synthesis of benzimidazole derivatives, Res. Chem. Intermed. 43 (2017) 1751–1766. https://doi.org/10.1007/s11164-016-2727-0.

[53] S. Shajari, E. Kowsari, N. Seifvand, F. Boorboor Ajdari, A. Chinnappan, S. Ramakrishna, G. Saianand, M. Dashti Najafi, V. Haddadi-asl, S. Abdpour, Efficient photocatalytic degradation of gaseous benzene and toluene over novel hybrid pil@tio2/m-go composites, Catalysts. 11 (2021) 1–24. https://doi.org/10.3390/catal11010126.

[54] L. Zu, X. Gao, H. Lian, X. Cai, C. Li, Y. Zhong, Y. Hao, Y. Zhang, Z. Gong, Y. Liu, X. Wang, X. Cui, High electrochemical performance phosphorus-oxide modified graphene electrode for redox supercapacitors prepared by one-step electrochemical exfoliation, Nanomaterials. 8 (2018) 417. https://doi.org/10.3390/nano8060417.

[55] M.R. Chirani, E. Kowsari, H. SalarAmoli, M. Yousefzadeh, A. Chinnappan, S. Ramakrishna, Covalently functionalized graphene oxide with cobalt–nitrogen-enriched complex containing iodide ligand as charge carrier nanofiller for eco-friendly high performance ionic liquid-based dye-sensitized solar cell, J. Mol. Liq. 325 (2021) 115198. https://doi.org/10.1016/j.molliq.2020.115198.

[56] J. Zhu, Z. Zhu, H. Zhang, H. Lu, W. Zhang, Y. Qiu, L. Zhu, S. Küppers, Calcined layered double hydroxides/reduced graphene oxide composites with improved photocatalytic degradation of paracetamol and efficient oxidation-adsorption of As(III), Appl. Catal. B Environ. 225 (2018) 550–562. https://doi.org/10.1016/j.apcatb.2017.12.003.

[57] V.K. Gupta, A. Fakhri, S. Agarwal, M. Naji, Palladium oxide nanoparticles supported on reduced graphene oxide and gold doped: Preparation, characterization and electrochemical study of supercapacitor electrode, J. Mol. Liq. 249 (2018) 61–65. https://doi.org/10.1016/j.molliq.2017.11.016.

[58] T. Jayabalan, M. Matheswaran, V. Preethi, S. Naina Mohamed, Enhancing biohydrogen production from sugar industry wastewater using metal oxide/graphene nanocomposite catalysts in microbial electrolysis cell, Int. J. Hydrogen Energy. 45 (2020) 7647–7655. https://doi.org/10.1016/j.ijhydene.2019.09.068.

[59] Y. Hou, Z. Wen, S. Cui, X. Guo, J. Chen, Constructing 2D porous graphitic C3N4 nanosheets/nitrogen-doped graphene/layered MoS2 ternary nanojunction with enhanced photoelectrochemical activity, Adv. Mater. 25 (2013) 6291–6297. https://doi.org/10.1002/adma.201303116.

[60] J. Bin Wu, M.L. Lin, X. Cong, H.N. Liu, P.H. Tan, Raman spectroscopy of graphene-

based materials and its applications in related devices, Chem. Soc. Rev. 47 (2018) 1822–1873. https://doi.org/10.1039/c6cs00915h.

[61] A.A. Ashtiani, E. Kowsari, V. Haddadi-Asl, M. Yousefi, H.R. Naderi, A. Chinnappan, S. Ramakrishna, Pseudocapacitive efficiency of covalently Cr-complex with L-histidine-methyl ester as a ligand graphene oxide blended with conducting polymer (POAP) as electrode material in supercapacitor, J. Mol. Liq. 315 (2020) 113697. https://doi.org/10.1016/j.molliq.2020.113697.

[62] T. Jayabalan, M. Manickam, S. Naina Mohamed, NiCo2O4-graphene nanocomposites in sugar industry wastewater fed microbial electrolysis cell for enhanced biohydrogen production, Renew. Energy. 154 (2020) 1144–1152. https://doi.org/10.1016/j.renene.2020.03.071.

[63] A. Lerf, H. He, M. Forster, J. Klinowski, Structure of graphite oxide revisited, J. Phys. Chem. B. 102 (1998) 4477–4482. https://doi.org/10.1021/jp9731821.

[64] E. Kowsari, A. Ehsani, M. Dashti Najafi, N. Seifvand, A.A. Heidari, Geminal dicationic ionic liquid functionalized graphene nanoribbon/POAP composite film: synthesis, characterization and electrochemical pseudocapacitance performance, Ionics (Kiel). 24 (2018) 2083–2092. https://doi.org/10.1007/s11581-018-2459-9.

[65] G.A.M. Ali, E. Megiel, P. Cieciórski, M.R. Thalji, J. Romański, H. Algarni, K.F. Chong, Ferrocene functionalized multi-walled carbon nanotubes as supercapacitor electrodes, J. Mol. Liq. 318 (2020) 114064. https://doi.org/10.1016/j.molliq.2020.114064.

[66] G.A.M. Ali, E. Megiel, J. Romański, H. Algarni, K.F. Chong, A wide potential window symmetric supercapacitor by TEMPO functionalized MWCNTs, J. Mol. Liq. 271 (2018) 31–39. https://doi.org/10.1016/j.molliq.2018.08.123.

[67] N.I. Chandrasekaran, H. Muthukumar, A.D. Sekar, A. Pugazhendhi, M. Manickam, High-performance asymmetric supercapacitor from nanostructured tin nickel sulfide (SnNi2S4) synthesized via microwave-assisted technique, J. Mol. Liq. 266 (2018) 649–657. https://doi.org/10.1016/j.molliq.2018.06.084.

[68] S.K. Shinde, D.-Y. Kim, V.G. Parale, H.-H. Park, H.M. Yadav, Electrochemically Synthesized Nanoflowers to Nanosphere-Like NiCuSe2 Thin Films for Efficient Supercapacitor Application, Metals (Basel). 10 (2020) 1698. https://doi.org/10.3390/met10121698.

[69] N. Li, Z. Xu, Y. Liu, Z. Hu, Hollow amorphous microspheres of nickel phosphate: Synthesis using adenosine 5″-triphosphate disodium salt as a new organic phosphorus source and their application as electrode materials in supercapacitors, J. Power Sources. 426 (2019) 1–10. https://doi.org/10.1016/j.jpowsour.2019.04.016.

[70] Y. He, Y. Zhang, X. Li, Z. Lv, X. Wang, Z. Liu, X. Huang, Capacitive mechanism of oxygen functional groups on carbon surface in supercapacitors, Electrochim. Acta. 282 (2018) 618–625. https://doi.org/10.1016/j.electacta.2018.06.103.

[71] N.I. Chandrasekaran, M. Manickam, Mesoporous hollow Mn Cu Al layered triple hydroxides nanocomposite synthesized via microwave assisted technique for symmetrical

supercapacitor, Int. J. Hydrogen Energy. 42 (2017) 26475–26487. https://doi.org/10.1016/j.ijhydene.2017.08.007.

[72] G.A.M. Ali, M.R. Thalji, W.C. Soh, H. Algarni, K.F. Chong, One-step electrochemical synthesis of MoS2/graphene composite for supercapacitor application, J. Solid State Electrochem. 24 (2020) 25–34. https://doi.org/10.1007/s10008-019-04449-5.

[73] G.A.M. Ali, M.M. Yusoff, H. Algarni, K.F. Chong, One-step electrosynthesis of MnO2/rGO nanocomposite and its enhanced electrochemical performance, Ceram. Int. 44 (2018) 7799–7807. https://doi.org/10.1016/j.ceramint.2018.01.212.

[74] A. Ehsani, E. Kowsari, M. Dashti Najafi, R. Safari, H. Mohammad Shiri, Influence of ionic liquid on pseudocapacitance performance of electrochemically synthesized conductive polymer: Electrochemical and theoretical investigation, J. Colloid Interface Sci. 500 (2017) 315–320. https://doi.org/10.1016/j.jcis.2017.04.014.

[75] A. Ehsani, E. Kowsari, F. Boorboor Ajdari, R. Safari, H. Mohammad Shiri, Influence of newly synthesized geminal dicationic ionic liquid on electrochemical and pseudocapacitance performance of conductive polymer electroactive film, J. Colloid Interface Sci. 505 (2017) 1158–1164. https://doi.org/10.1016/j.jcis.2017.07.001.

[76] S.K. Shinde, H.M. Yadav, S. Ramesh, C. Bathula, N. Maile, G.S. Ghodake, H. Dhaygude, D.-Y. Kim, High-performance symmetric supercapacitor; nanoflower-like NiCo2O4//NiCo2O4 thin films synthesized by simple and highly stable chemical method, J. Mol. Liq. 299 (2020) 112119. https://doi.org/10.1016/j.molliq.2019.112119.

[77] S.K. Shinde, M.B. Jalak, S.Y. Kim, H.M. Yadav, G.S. Ghodake, A.A. Kadam, D.-Y. Kim, Effect of Mn doping on the chemical synthesis of interconnected nanoflakes-like CoS thin films for high performance supercapacitor applications, Ceram. Int. 44 (2018) 23102–23108. https://doi.org/10.1016/j.ceramint.2018.09.117.

[78] H.M. Yadav, G.S. Ghodake, D.-Y. Kim, S. Ramesh, N.C. Maile, D.S. Lee, S.K. Shinde, Nanorods to hexagonal nanosheets of CuO-doped manganese oxide nanostructures for higher electrochemical supercapacitor performance, Colloids Surfaces B Biointerfaces. 184 (2019) 110500. https://doi.org/10.1016/j.colsurfb.2019.110500.

[79] J. Jose, S. Jose, S. Abinaya, S. Shaji, P.B. Sreeja, Benzoyl hydrazine-anchored graphene oxide as supercapacitor electrodes, Mater. Chem. Phys. 256 (2020). https://doi.org/10.1016/j.matchemphys.2020.123666.

[80] C. Li, J. Yang, P. Pachfule, S. Li, M.Y. Ye, J. Schmidt, A. Thomas, Ultralight covalent organic framework/graphene aerogels with hierarchical porosity, Nat. Commun. 11 (2020). https://doi.org/10.1038/s41467-020-18427-3.

[81] Y. Xu, X. Li, G. Hu, T. Wu, Y. Luo, L. Sun, T. Tang, J. Wen, H. Wang, M. Li, Graphene oxide quantum dot-derived nitrogen-enriched hybrid graphene nanosheets by simple photochemical doping for high-performance supercapacitors, Appl. Surf. Sci. 422 (2017) 847–855. https://doi.org/10.1016/j.apsusc.2017.05.189.

[82] F. Jiang, J. Zhang, N. Li, C. Liu, Y. Zhou, X. Yu, L. Sun, Y. Song, S. Zhang, Z. Wang, Nitrogen-doped graphene prepared by thermal annealing of fluorinated graphene oxide as

supercapacitor electrode, J. Chem. Technol. Biotechnol. 94 (2019) 3530–3537. https://doi.org/10.1002/jctb.6147.

[83] H. Wang, Q. Fu, C. Pan, Green mass synthesis of graphene oxide and its MnO2 composite for high performance supercapacitor, Electrochim. Acta. 312 (2019) 11–21. https://doi.org/10.1016/j.electacta.2019.04.178.

[84] P. Ramesh, B. Jebasingh, A facile synthesis of bis-(ptththalimidoethyl)-amine functionalized graphene oxide and its dual performance as a supercapacitor electrode and fluorescence sensor, Mater. Chem. Phys. 222 (2019) 45–54. https://doi.org/10.1016/j.matchemphys.2018.09.075.

[85] P. Ramesh, S. Amalraj, P. Arunachalam, M. Gopiraman, A.M. Al-Mayouf, S. Vasanthkumar, Covalent intercalation of hydrazine derived graphene oxide as an efficient 2D material for supercapacitor application, Synth. Met. 272 (2021) 116656. https://doi.org/10.1016/j.synthmet.2020.116656.

[86] M. Bonakdar, S.R. Hosseini, S. Ghasemi, Poly(o-Anisidine)/carbon nanotubes/graphene nanocomposite as a novel and cost-effective supercapacitor material, Mater. Sci. Eng. B Solid-State Mater. Adv. Technol. 267 (2021) 115099. https://doi.org/10.1016/j.mseb.2021.115099.

[87] S. Ramanathan, M. SasiKumar, N. Radhika, A. Obadiah, A. Durairaj, G. Helen Swetha, P. Santhoshkumar, I. Sharmila Lydia, S. Vasanthkumar, Musa paradisiaca reduced graphene oxide (BRGO) /MWCNT-Fe3O4 nanocomposite for supercapacitor and photocatalytic applications, Mater. Today Proc. (2021). https://doi.org/10.1016/j.matpr.2021.01.706.

[88] Q. Wang, H. Gao, C. Zhao, H.X. Yue, G. Gao, J. Yu, Y.U. Kwon, Y. Zhao, Covalent modified reduced graphene oxide: Facile fabrication and high rate supercapacitor performances, Electrochim. Acta. 369 (2021) 137700. https://doi.org/10.1016/j.electacta.2020.137700.

[89] E. Kowsari, A. Ehsani, M. Dashti Najafi, Electrosynthesis and pseudocapacitance performance of ionic liquid – Cr (η6-C6H5) complex functionalized reduced graphene oxide/poly ortho aminophenol nanocomposite film, J. Colloid Interface Sci. 504 (2017) 507–513. https://doi.org/10.1016/j.jcis.2017.05.117.

[90] F. Boorboor Ajdari, M. Dashti Najafi, M. Izadpanah Ostad, H. reza Naderi, M. Niknam Shahrak, E. Kowsari, S. Ramakrishna, A symmetric ZnO-ZIF8//Mo-ZIF8 supercapacitor and comparing with electrochemical of Pt, Au, and Cu decorated ZIF-8 electrodes, J. Mol. Liq. 333 (2021) 116007. https://doi.org/10.1016/j.molliq.2021.116007.

[91] S. Pilathottathil, T. Kannan Kottummal, M.S. Thayyil, P. Mahadevan Perumal, J. Ambichi Purakakath, Inorganic salt grafted ionic liquid gel electrolytes for efficient solid state supercapacitors: Electrochemical and dielectric studies, J. Mol. Liq. 264 (2018) 72–79. https://doi.org/10.1016/j.molliq.2018.05.014.

[92] R. Zarrougui, R. Hachicha, R. Rjab, O. Ghodbane, 1-Allyl-3-methylimidazolium-based ionic liquids employed as suitable electrolytes for high energy density supercapacitors based on graphene nanosheets electrodes, J. Mol. Liq. 249 (2018) 795–804. https://doi.org/10.1016/j.molliq.2017.11.078.

[93] H. Muthukumar, S.N. Mohammed, N. Chandrasekaran, A.D. Sekar, A. Pugazhendhi, M. Matheswaran, Effect of iron doped Zinc oxide nanoparticles coating in the anode on current generation in microbial electrochemical cells, Int. J. Hydrogen Energy. 44 (2019) 2407–2416. https://doi.org/10.1016/j.ijhydene.2018.06.046.

[94] S.T. Gunday, E. Cevik, I. Anil, O. Alagha, H. Sabit, A. Bozkurt, Symmetric Supercapacitor Application of Anhydrous Gel Electrolytes Comprising Doped Tetrazole Terminated Flexible Spacers, Macromol. Res. 28 (2020) 1074–1081. https://doi.org/10.1007/s13233-020-8150-9.

[95] N.I. Chandrasekaran, H. Muthukumar, A.D. Sekar, M. Manickam, Hollow nickel-aluminium-manganese layered triple hydroxide nanospheres with tunable architecture for supercapacitor application, Mater. Chem. Phys. 195 (2017) 247–258. https://doi.org/10.1016/j.matchemphys.2017.04.027.

[96] J. Du, A. Chen, L. Liu, B. Li, Y. Zhang, N-doped hollow mesoporous carbon spheres prepared by polybenzoxazines precursor for energy storage, Carbon N. Y. 160 (2020) 265–272. https://doi.org/10.1016/j.carbon.2020.01.018.

[97] J. Du, Y. Zhang, H. Lv, A. Chen, N/B-co-doped ordered mesoporous carbon spheres by ionothermal strategy for enhancing supercapacitor performance, J. Colloid Interface Sci. 587 (2021) 780–788. https://doi.org/10.1016/j.jcis.2020.11.037.

[98] Y. Mo, J. Du, H. Lv, Y. Zhang, A. Chen, N-doped mesoporous carbon nanosheets for supercapacitors with high performance, Diam. Relat. Mater. 111 (2021) 108206. https://doi.org/10.1016/j.diamond.2020.108206.

[99] N. Neekzad, E. Kowsari, M.D. Najafi, H. Reza Naderi, A. Chinnappan, S. Ramakrishna, V. Haddadi-Asl, Pseudocapacitive performance of surface functionalized halloysite nanotubes decorated green additive ionic liquid modified with ATP and POAP for efficient symmetric supercapacitors, J. Mol. Liq. (2021) 116962. https://doi.org/10.1016/j.molliq.2021.116962.

[100] Z. Shen, Y. Mo, J. Du, A. Chen, Nitrogen-enriched hierarchically porous carbon sheets anchored with ZIF-derived carbon for supercapacitors, Appl. Surf. Sci. 527 (2020) 146845. https://doi.org/10.1016/j.apsusc.2020.146845.

[101] J. Du, S. Zong, Y. Zhang, S. Hou, A. Chen, Co-assembly strategy for uniform and tunable hollow carbon spheres with supercapacitor application, J. Colloid Interface Sci. 565 (2020) 245–253. https://doi.org/10.1016/j.jcis.2020.01.021.

[102] Y. Liu, D. He, H. Wu, J. Duan, Y. Zhang, Hydrothermal Self-assembly of Manganese Dioxide/Manganese Carbonate/Reduced Graphene Oxide Aerogel for Asymmetric Supercapacitors, Electrochim. Acta. 164 (2015) 154–162. https://doi.org/10.1016/j.electacta.2015.01.223.